

MAGNETIC RECONNECTION TURBULENCE IN STRONG GUIDE FIELDS: BASIC PROPERTIES AND APPLICATION TO CORONAL HEATING

M. J. PUESCHEL¹, D. TOLD², P. W. TERRY¹, F. JENKO^{2,3}, E. G. ZWEIBEL¹, V. ZHDANKIN¹, AND H. LESCH⁴

¹ Center for Magnetic Self-Organization, University of Wisconsin-Madison, Madison, WI 53706, USA

² Max-Planck-Institut für Plasmaphysik, D-85748 Garching, Germany

³ Max-Planck/Princeton Center for Plasma Physics

⁴ Universitätssternwarte München, D-81679 München, Germany

Received 2014 May 9; accepted 2014 June 23; published 2014 July 23

ABSTRACT

A current sheet susceptible to the tearing instability is used to drive reconnection turbulence in the presence of a strong guide field. Through nonlinear gyrokinetic simulations, the dependencies of central quantities such as the heating rate on parameters like collisionality or plasma β are studied, revealing that linear physics tends to predict only some aspects of the quasi-saturated state, with the nonlinear cascade responsible for additional features. For the solar corona, it is demonstrated that the kinetic heating associated with this type of turbulence agrees quantitatively with observational volumetric heating rates. In the context of short particle acceleration events, the self-consistent emergence of plasmoids or flux ropes in the turbulent bath is found to be important: ubiquitously occurring merger events of these objects cause strong bursts in the heating rate, the timescale of which is consistent with nanoflare observations. Furthermore, anisotropy of the temperature fluctuations is seen to emerge, hinting at a new means of generating coronal ion temperature anisotropy in the absence of cyclotron resonances.

Key words: acceleration of particles – magnetic reconnection – plasmas – Sun: corona – turbulence

Online-only material: color figures

1. INTRODUCTION

The physics underlying magnetic reconnection processes have been the center of significant attention. One of the most pressing questions relates to coronal heating: can reconnection events provide enough particle acceleration to explain the still insufficiently understood phenomenon of coronal spectra extending to very high energies? Zweibel & Yamada (2009) contains an overview of reconnection physics, including a list of open questions; additionally, a number of encompassing review papers exists on the topic, recent examples of which include Yamada et al. (2010), Cassak & Shay (2012), Lazarian et al. (2012), Karimabadi et al. (2013), and Paschmann et al. (2013). For a review of coronal particle acceleration physics, including reconnection-based heating, the reader is directed to Zharkova et al. (2011).

Another important issue is the observation of ion temperature anisotropy in the corona, which favors perpendicular temperatures and is typically explained through cyclotron resonances (Marsch et al. 1982; Kohl et al. 1997, 1998; Cranmer 2001; von Steiger & Zurbuchen 2003). In contrast, the present approach focuses on how lower-frequency processes may influence temperature anisotropy.

Simulation-based studies of reconnection (see Donato et al. 2013 for an overview) can mostly be divided into fluid (Neukirch 1996; Ottaviani et al. 2004; Loureiro et al. 2009; Servidio et al. 2009; Fitzpatrick 2010; Grasso et al. 2010; Zweibel et al. 2011; Rappazzo & Velli 2011; Comisso et al. 2012) and kinetic (Hesse et al. 1999; Swisdak et al. 2003; Pritchett 2006; Wang et al. 2008; Drake et al. 2009; Daughton et al. 2009; Loureiro et al. 2013) approaches. The latter, while utilizing a more complete physical framework, require large—sometimes prohibitively so—amounts of computational resources, particularly when the reconnecting field is much smaller than the guide field. In the fusion community, where plasmas are strongly magnetized, a popular and well-benchmarked tool for the study of kinetic

effects is gyrokinetics, which has also been used to address various astrophysical problems (see, e.g., Schekochihin et al. 2009). A moderate number of gyrokinetic studies of space-physics-relevant tearing modes exists (Wan et al. 2005; Rogers et al. 2007; Perona et al. 2010; Pueschel et al. 2011; Numata et al. 2011; Zacharias et al. 2012; Ishizawa & Watanabe 2013; Kobayashi et al. 2014), most of which cover only linear physics or the onset of nonlinearity, but not fully developed turbulence. It is therefore essential that the nonlinear physics be investigated in detail and that comparisons be made that relate linear and nonlinear scalings and features. Existing gyrokinetic simulations of turbulent reconnection tend to focus on reconnection events occurring in otherwise created turbulent fields, e.g., via the excitation of Alfvén waves (TenBarge & Howes 2013). The aim of the present work is to drive reconnection through a current sheet and then study—motivated primarily by solar corona physics—particle acceleration and heating as a consequence of both the direct impact of the sheet and of secondary reconnection events; look for the possible formation of temperature anisotropies; and, more generally, comment on the similarities and differences between linear and nonlinear physics in the simulations. It is worth reiterating that using this approach, turbulence arises from the linear tearing mode drive and then, in turn, causes a constant barrage of secondary reconnection events.

One aspect of secondary reconnection is the plasmoid instability. This process, which has been amply discussed in the literature (Biskamp 1986; Drake et al. 2006; Loureiro et al. 2007; Fermo et al. 2012; Huang & Bhattacharjee 2013; Cassak & Drake 2013), describes a critical breaking-up of an elongated current sheet into filaments of roughly circular cross-sections called plasmoids and occurs at high Lundquist numbers. Its rates are super-Alfvénic, and it creates an environment in which different plasmoids may interact and merge. In the present paper, the turbulent bath and the current sheet similarly birth circular structures that turn out to be rather important to heating, and

connections with the standard picture of the plasmoid instability are made.

In Pueschel et al. (2011), building on previous work (Porcelli 1991; Rogers et al. 2007), linear reconnection studies were undertaken that describe the variation of the reconnection rate with all relevant physical input parameters, followed by initial studies of both decaying and driven reconnection turbulence. The latter topic—quasi-stationary turbulence driven by a continuously replenishing, reconnecting current sheet—is the focus of the present paper, which is structured as follows. A brief review of the underlying (linear) tearing mode physics is given in Section 2, along with a description of gyrokinetics, the Vlasov equation on which this work is based, and a few details on the numerical implementation; the standard set of physical parameters used throughout most of this work is specified there as well. Section 3 then focuses on the initial condition, which models current sheets and is simultaneously used in the Krook-type drive term. In Section 4, in-depth analyses of reconnection turbulence are presented, with the central areas of focus being the description of the properties of the observed turbulence; parametric dependencies of central quantities, such as the parallel electric field, and the relation of these dependencies to linear physics; the occurrence of coherent circular structures referred to as plasmoids and merger events of the same; and the comparison of collisional versus kinetic heating. Anisotropies between parallel and perpendicular temperature fluctuations are the subject of Section 5. In Section 6, parameters relevant to plasmas in the solar corona are applied to the simulations, enabling a quantitative comparison between observations and central results of the simulation studies in the present work. This is followed by a summary of the findings of this paper.

2. ANALYTICAL BACKGROUND AND NUMERICAL FRAMEWORK

The tearing mode, a process of magnetic reconnection, is a plasma instability that depletes free magnetic energy from a current gradient by reorienting the magnetic field structure corresponding to said current (see, e.g., Furth et al. 1963). It relies on some form of resistivity, supplied either by collisionality, as in a fluid picture, or electron inertia/pressure, as in a kinetic picture. In the present work, the focus lies on sinusoidal current sheets, which have been amply described in Porcelli (1991), Rogers et al. (2007), and Pueschel et al. (2011), for which the usual tearing mode stability parameter becomes

$$\Delta' = 2k_x \left(1 - \frac{k_y^2}{k_x^2}\right)^{1/2} \tan \left[\frac{\pi}{2} \left(1 - \frac{k_y^2}{k_x^2}\right)^{1/2} \right]. \quad (1)$$

Here $k_{x,y}$ are wave numbers in the directions perpendicular to the uniform background magnetic field B_0 (along which the coordinate z is defined, normalized to the macroscopic length L_{ref} , which can be thought of as the length of a coronal loop; in the following, derivatives along z are dropped). Both k_x and k_y are normalized to the inverse of the ion sound gyroradius $\rho_s = c_s m_i c / (e B_0)$, which coincides with the ion gyroradius for equal background temperatures $T_{i0} = T_{e0}$ of the ions and electrons. Here the following quantities have been introduced: the ion sound speed $c_s = (T_{e0}/m_i)^{1/2}$, the ion mass m_i , the speed of light c , and the elementary charge e . The reconnecting field $B_{y0} \equiv B_y(t=0) \propto \sin k_{cs} x$ is imposed at a single driving $k_x = k_{cs} \equiv 2\pi/\lambda_{cs}$ (with $k_y = 0$; one may think of λ_{cs} as a shear

length), inducing tearing mode growth in the range $k_y \in]0, k_{cs}[$, corresponding to $\Delta' \in]\infty, 0[$.

In the present paper, this physical setup is studied using the gyrokinetic framework (Frieman & Chen 1982; Brizard & Hahm 2007). Unlike their kinetic equivalents, gyrokinetic codes are not able to capture cyclotron or compressional Alfvén waves, due to their high frequencies. In gyrokinetics, the fast cyclotron motion of particles about field lines is ordered out, effectively eliminating one velocity space coordinate and thus significantly enhancing numerical efficiency. The assumptions made to arrive at the gyrokinetic equations are as follows: due to the large background magnetic field, the Larmor frequency of any of the fully ionized particle species is much larger than any frequencies of interest for a given system, such as frequencies of plasma instabilities, and any background length scales, such as the variation scales of the background magnetic field L_B or of the background density/temperature gradients $L_{n,T}$, are much larger than the Larmor radius ρ . Therefore, while not applicable in cases of weak magnetization, gyrokinetics makes the study of collisionless or moderately collisional reconnection in strong guide fields feasible, with the reconnecting field $B_{\text{rec}} \ll B_0$, which are particularly difficult to simulate for kinetic codes due to the implied scale separation. A recent publication (TenBerge et al. 2014) compares results from gyrokinetic and kinetic codes, where the latter use a strong guide field of varying amplitude, and concludes that good agreement between the two approaches can be reached for a wide range of settings. Gyrokinetic codes have been used to study a number of space- and astrophysical systems; examples are referenced throughout this paper.

The reader's attention is now directed to the numerical implementation and central equation used in this work. All numerical results in this paper are based on the nonlinear gyrokinetic Vlasov solver GENE⁵ (Jenko et al. 2000). Its capabilities with respect to reconnection physics are discussed in detail in Pueschel et al. (2011), but a small change in the Krook drive term of the Vlasov equation has since been introduced; the new Vlasov equation reads

$$\frac{\partial g_j}{\partial t} = \sum_{k'} (k'_x k_y - k_x k'_y) \chi(k') g_j(k - k') - \omega_{\text{dr}} \times (g_j(k_y = 0, t) - g_j(k_y = 0, t = 0)) + \left. \frac{\partial f_j}{\partial t} \right|_{\text{coll}}, \quad (2)$$

where the terms on the right side, in order, correspond to the $E \times B$ nonlinearity (through which the linear tearing mode is receiving energy from the current sheet), the Krook-type drive term, and the collision term; the parallel nonlinearity (Candy et al. 2006) can be ignored for $L_{\text{ref}}/\rho_s \gtrsim 100$. The quantities introduced here are the modified perturbed distribution function $g_j = f_j + 2q_j v_{\parallel} \bar{A}_{\parallel j} F_{j0} / (m_j v_{Tj})$ of species j , defined relative to the perturbed distribution function f_j ; the time t in units of L_{ref}/c_s ; the generalized potential $\chi = \bar{\Phi}_j - v_{Tj} v_{\parallel} \bar{A}_{\parallel j} + (T_{j0}/q_j) \mu \bar{B}_{\parallel j}$; and the charge q_j . Furthermore, the background distribution function F_{j0} is uniform in space and a simple Maxwellian in velocity space, $F_{j0} = \pi^{-3/2} \exp(-v_{\parallel}^2 - \mu B_0)$, and overbars denote (species-dependent) gyroaverages. The Vlasov equation is complemented by field equations for the electrostatic potential Φ , the parallel magnetic vector potential A_{\parallel} , and (perturbed) parallel magnetic field B_{\parallel} , which can be found in Pueschel et al. (2011). The Debye length, being much

⁵ For code access and details, see <http://gene.rzg.mpg.de>.

smaller than the scales investigated throughout this paper, is set to zero. Additionally, the following definitions are used: ω_{dr} is the nonlinear drive frequency; $v_{Tj} = (2T_{j0}/m_j)^{1/2}$ is the thermal velocity to which the parallel velocity coordinate v_{\parallel} is normalized; and $\mu = m_j v_{Tj}^2 / (2B_0)$ is the magnetic moment coordinate, normalized to v_{Tj}^2 . While it may appear counterintuitive that the formally linear Krook drive term and its associated frequency are referred to as *nonlinear*, this label refers to their role in driving nonlinear, turbulent simulations, whereas linear tearing mode simulations (which, ironically, rely on the Vlasov nonlinearity) require no replenishing of the current sheet.

Equation (2) does not incorporate variations along the direction along the magnetic field. Preliminary simulation results indicate, however, that fully resolving (with, in general, $\partial_z \neq 0$) that coordinate—while not adding helicity to the driving current sheet—does not alter the linear results significantly; note that for these simulations, the strength of the parallel current also depends on z . Using the present, reduced setup where $\partial_z \equiv 0$ is therefore justified as long as the current sheets under investigation conform with the requirements implied above. Note also that the effective use of periodic as opposed to line-tied parallel boundary conditions (Einaudi & Van Hoven 1981) can be motivated by assuming that, say, in a coronal loop, the nonlinear plasma state that serves as the equilibrium of microturbulence studies should be largely independent of the parallel boundary conditions.

The default set of physical parameters used throughout most of this paper is as follows: the k_x wave number $k_{cs} = 0.4$ at which the current sheet is initialized; the electron pressure $\beta \equiv \beta_e \equiv 8\pi n_{e0} T_{e0} / B_0^2 = 0.5$, with the electron background density $n_{e0} \equiv n_{i0}$; equal ion and electron temperatures: $T_{i0} = T_{e0}$ (and thus $\beta_e + \beta_i = 1$); the mass ratio $m_e/m_i = 0.01$, a setting used to lower simulation cost; and lastly, the driving frequency $\omega_{\text{dr}} = 0.1$, normalized to c_s/L_{ref} ; see Section 3. Also in that section is a description of the current sheet setup, which is produced through an x -dependent, sinusoidal shift of the perturbed electron distribution function in the parallel velocity, which along x has a maximum of $\Delta v_{\parallel} = 0.5$. The following dimensionless definition is used for the collision frequency, with all constituting quantities normalized to cgs units:

$$v_c = 3.1 \times 10^{-6} \frac{n_{e0} L_{\text{ref}}}{T_{e0}^2} \left[24 - \ln \left(\frac{n_{e0}^{1/2}}{8.6 \times 10^{-5} T_{e0}} \right) \right]. \quad (3)$$

The term in the square brackets is the usual Coulomb logarithm. The default setting of the collisionality is $v_c = 0.005$, which translates to $v_{ei} = 0.02(m_i/m_e)^{1/2}$ in units of c_s/L_{ref} . All binary collision types are retained in the collision operator.

As the standard numerical settings for reconnection turbulence simulations in this paper, the following values are selected: 128×64 complex modes in $x \times y$ (corresponding to 128×128 grid points in real space, or 192×192 when taking into account anti-aliasing in the Vlasov nonlinearity), spanning a periodic square box with edges $20\pi\rho_s$ long, and 32×8 grid points in $v_{\parallel} \times \mu$, spanning a velocity space of $-3v_{Tj} \dots 3v_{Tj}$ and $0 \dots 9v_{Tj}^2$, respectively. Convergence tests were performed successfully in all these parameters for the standard nonlinear (i.e., turbulence) case. Additionally, convergence was ensured separately in the x box size and resolution when scanning various physical parameters. Note that as $k_{cs} = 0.4$ is fixed, the default box contains four current sheets, while increasing the box size for convergence testing adds more current sheets (along with

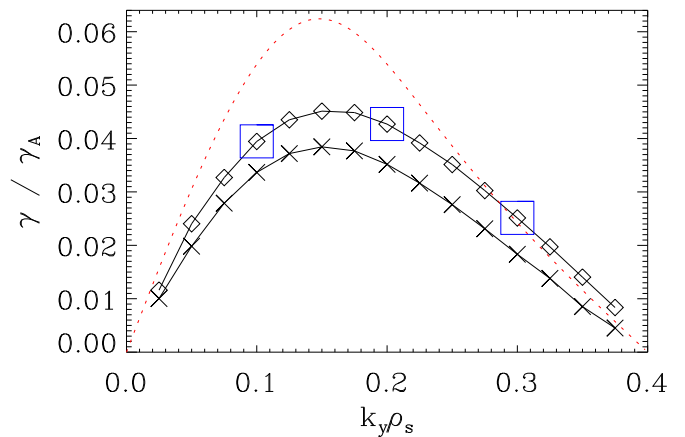


Figure 1. Linear tearing mode growth rates for the standard parameter set, normalized to the inverse Alfvén time: crosses are collisionless data, and diamonds have the default v_c . Shown as a red dotted curve, the analytical solution of the (collisionless) dispersion relation does not capture the physics very accurately anymore for this case. Marked with blue squares are the k_y values that are included in the turbulent case, which, in particular, reasonably cover the range of most unstable wave numbers.

(A color version of this figure is available in the online journal.)

grid points in x). All quantities are presumed to be constant in the real-space direction z , which is parallel to the (unperturbed) magnetic field.

Analytical theory (Porcelli 1991) yields good predictions for the limits $k_y \rightarrow 0$ and $k_y \rightarrow k_{cs}$, as long as certain conditions are fulfilled with respect to the total normalized plasma pressure $\beta_{\text{tot}} = \beta_e + \beta_i = \beta(1 + T_{i0}/T_{e0})$ and the mass ratio m_e/m_i ; see Pueschel et al. (2011); Rogers et al. (2007, 2011) (where it was necessary to use a cold-ion limit to achieve good agreement). For the physical parameters under consideration in the present work, spectra of the tearing mode growth rate γ are shown in Figure 1, with the full dispersion relation solution—as was also done in Comisso et al. (2013)—included as a red dotted line. The latter exceeds the numerical results by a few tens of percent, in part due to the finite ion temperature, and should only be used for order-of-magnitude estimates for the present parameter case. Note that the analytical curve in this figure does not include corrections due to finite collisionality (which slightly increase γ); a discussion of the applicability of the corrections in Porcelli (1991) can be found in Pueschel et al. (2011); however, the collisional simulation data points have been adjusted to compensate for the slow collisional decay of the current sheet with time.

While for linear results in Pueschel et al. (2011) and in Figure 1, growth rates are normalized to the inverse Alfvén time, which in units of c_s/L_{ref} reads

$$\gamma_A = \frac{k_{cs} B_{y0,\text{max}}}{(n_{e0} m_i)^{1/2}} \left(\frac{2}{\beta} \right)^{1/2}, \quad (4)$$

the turbulence studies, as well as any additional linear results, in this paper use c_s and L_{ref} as normalization, unless specified otherwise. The quantity $B_{y0,\text{max}} \equiv 2^{1/2} B_{\text{rec}}$ introduced above corresponds to the maximum along x of the magnetic field perturbation $B_y = -\partial_x A_{\parallel}$ at time $t = 0$ (note that B_{\parallel} does not enter into B_y , as it involves $\partial_z \ll \partial_x$); for default parameters, $B_{y0,\text{max}} = 5.107$ in units of $B_0 \rho_s / L_{\text{ref}}$.

In order to facilitate straightforward comparisons with fluid approaches, it is helpful to convert the collisionality v_c into the Lundquist number S . For gyrokinetic systems with a sinusoidal

current sheet, the latter can be expressed as (Numata et al. 2011)

$$S = 13.0 \frac{\gamma_A \beta (m_i/m_e)^{1/2}}{v_c k_{cs}^2}, \quad (5)$$

which effectively reduces to

$$S = 18.4 \frac{B_{y0,\max} (\beta m_i/m_e)^{1/2}}{v_c k_{cs}}. \quad (6)$$

For the default set of parameters, this prescription yields $S = 3.32 \times 10^5$. With the largest value $v_c = 0.5$ used in this paper, S lies somewhat below 10^4 , an empirical threshold for multi-X-line reconnection (Cassak & Drake 2013) stemming from the usual inflow–outflow reconnection setups. To what extent this criterion is applicable here shall be one of the questions addressed in Section 4. Note also that the reconnection phase diagrams in Cassak & Drake (2013) put the present parameter case deeply into the Hall reconnection regime.

As indicated by the blue squares, only a subset of the modes shown in Figure 1 is included in the turbulence simulations. Since the linear physics require steeply rising x resolution as k_y approaches k_{cs} (i.e., when $\Delta' \rightarrow 0$), it is unfeasible to completely resolve the whole linear range shown in the figure. Instead, the lowest finite k_y is chosen as 0.1, and a larger number of k_y modes, all of which are linearly stable, are added at higher k_y to cover the turbulent cascade. As is confirmed by nonlinear convergence studies, the relevant linear physics—mostly in the form of the fastest-growing wave numbers—is still captured rather well, quantitatively. It should also be remarked that the resolution in x required to yield converged simulations is slightly lower for the turbulent case than it is for the linear growth rates. The reason is likely related to the fact that the turbulent cascade is largely independent of the driving wave numbers, and it contributes significantly to quantities such as the parallel electric field.

One aspect of the numerical implementation central to this study is the drive term, along with the initial condition, both of which shall be discussed in the next section.

3. PHYSICAL INITIAL CONDITION AND DRIVE

As mentioned above, the initial state of the perturbed distribution is used in the drive term of the Vlasov equation as part of a new equilibrium and as a source of free energy. This property differs somewhat from gyrokinetic flux-tube simulations of fusion plasmas, where the quasi-stationary saturated state tends to be independent of the initial condition.

To construct the initial perturbed distribution function, an isotropic Maxwellian velocity space is shifted along v_{\parallel} , with the shift $-\Delta v_{\parallel} \cos k_{cs} x$ (for the electrons; opposite sign for the ions) depending on the spatial position; since Δv_{\parallel} is normalized to v_{Tj} , the lighter and faster electrons carry almost the entire current of the sheet. A current gradient is thus created along the x direction. A small perturbation δn_j is now added to the (perturbed) density n_j , such that $\delta n_j \ll n_j \ll n_{j0}$ for species j ; the additional perturbation is much smaller than the density associated with the perturbed distribution function f_j , which in turn is much smaller than the background density n_{j0} . The value selected is $\delta n_j/n_j = 10^{-3}$ for the nonlinear cases (linear simulations profit from a far smaller fraction). Figure 2 illustrates this initial condition, showing the magnetic potential A_{\parallel} .

Unlike in many other reconnection studies, the current sheets used here are in immediate proximity to each other, the motivation being that multiple periodic current sheets are included in

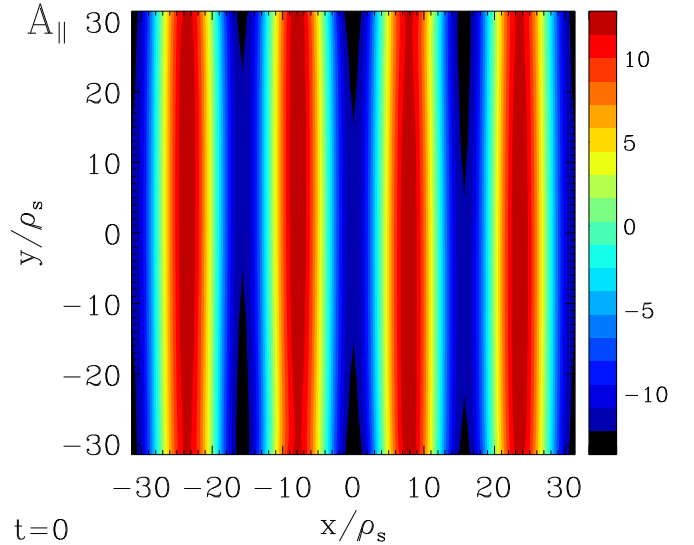


Figure 2. Initial condition: contours of the magnetic potential A_{\parallel} in the perpendicular plane. Four current sheets are subjected to a small but visible perturbation, leading to tearing mode growth in $0 < k_y < k_{cs}$. The $k_y = 0$ mode of the system is then continuously forced back toward this initial condition to inject energy in the absence of background pressure gradients. A_{\parallel} is given in units of $B_0 \rho_s^2 / L_{\text{ref}}$.

(A color version of this figure is available in the online journal.)

the simulation box in order to capture inverse cascade effects that stretch to lower $k_x < k_{cs}$. Therefore, important differences exist with regard to projected structure formation—more separated current sheets would likely see coherent structures form locally, with less interaction between structures in different sheets. Conversely, plasmoid chains created by directly neighboring current sheets will interact immediately across sheets. The present setup can be considered more suitable for investigating fully turbulent reconnection where structures are present more or less uniformly throughout the domain.

The drive term in Equation (2) forces the distribution, at a frequency of ω_{dr} , back to the original state at $t = 0$, but only for $k_y = 0$; the current sheet lives on that wave number, whereas the tearing mode as well as the turbulent cascade in k_y have $k_y > 0$. Thus, the current sheet, which would otherwise undergo quasilinear depletion, is continuously replenished at a timescale of $\tau_{\text{repl}} \equiv \omega_{\text{dr}}^{-1}$. This allows for a quasi-stationary state to develop, where energy is injected through the current sheet, processed by nonlinear dynamics, and eventually dissipated (or possibly even reabsorbed by the current sheet).

In the limit of small ω_{dr} —relative to the characteristic frequencies of the system—the restoring force on $f_j(k_y = 0)$ becomes small, and the system will take on the properties of decaying turbulence, including an inverse cascade of magnetic energy (Pueschel et al. 2011). Conversely, for very large ω_{dr} , the $k_y = 0$ mode will remain almost completely fixed to the initial condition. For this case, the turbulent cascade will be affected only indirectly, as the $k_y = 0$ mode enters into nonlinear coupling and therefore into the process underlying energy transfer.

When left to decay freely with the tearing mode suppressed, the current sheet dissipates collisionally on a timescale of $\tau_{\text{decay}} \approx 2000$ (for the default v_c), which is much longer than the dynamical timescales, as will be evident by comparison with the results in Section 4. For the purpose of quantifying the decay timescale, the perturbation $\delta n_j/n_j$ was set to a very small value, and only one finite- k_y mode was included at near-zero k_y .

In Pueschel et al. (2011), a very similar initial condition was used to study both decaying and driven turbulence. For the latter case, however, a different drive term was employed that involved the absolute value of the drive term in Equation (2). As a result, it is difficult to compare the two approaches directly. The next section presents in-depth analyses of the more realistic turbulence created by the new drive form.

4. RECONNECTION TURBULENCE

The aforementioned physical and numerical setup is now used to study the properties of the ensuing reconnection turbulence. Before discussing heating processes, a number of diagnostics are used for characterization.

4.1. Turbulence Characteristics

Tearing mode growth quickly breaks up the coherent structures that dominate the initial state (which was shown in Figure 2). In Figure 3, the beginning of the nonlinear phase is illustrated: the current sheets are starting to break up, but the fully turbulent state has not yet been reached. In addition to A_{\parallel} , the figure also includes the (perturbed) parallel electron flow speed $u_{\parallel e}$ —obtained via taking the v_{\parallel} moment of f_e —in units of $c_s \rho_s / L_{\text{ref}}$.

At a later time, the picture has changed fundamentally—see Figure 4, where contours are taken exemplarily at $t = 260$, representative of the quasi-stationary saturated state. Now circular coherent structures have formed that slowly drift in the perpendicular plane and may interact with one another or with current filaments through $j \times B$ forces. Based on their geometric properties, they will henceforth be referred to as *plasmoids* (Drake et al. 2006), although one may equivalently think of them as *flux ropes* (Lazarian et al. 2011; Daughton et al. 2011) that exhibit no variation along the background field. Analyses involving these plasmoids are presented in various places throughout this paper.

As some of the filaments, particularly ring-shaped ones encircling plasmoids, have a width not much larger than the grid spacing, it needs to be stressed that they are numerically resolved; at higher resolution (in both x and y), those filaments do not change their characteristic shapes or amplitudes.

It is instructive to also study time-averaged contours of A_{\parallel} and $u_{\parallel e}$, as provided in Figure 5; here the initial, transient phase of the simulation was excluded, and time averaging was done only over the quasi-stationary state. The magnetic potential shows to have undergone an inverse cascade, much like the decaying turbulence described in Pueschel et al. (2011), and it is therefore important to reiterate that these simulations are converged in the box size. On the other hand, $u_{\parallel e}$ shows significant contributions both at the smallest k_y as well as $k_x = k_{cs}$. The latter is unsurprising, as the current sheets inherently produce potential wells that attract coherent structures—most importantly, plasmoids—to these locations. As a comparison of the color bars in Figures 4 and 5 illustrates, however, the most prominent filaments and plasmoids far exceed the averaged structures in terms of their amplitudes.

As one central property of the tearing mode is to rearrange the magnetic field and reduce its free energy through isotropization, a closer look is taken at the perturbed B_x and B_y in Figure 6. During the magnified linear phase at $t \lesssim 10$, the emerging B_x depletes B_y , which stems from the current sheet. Once saturation is achieved, these components are almost equal in amplitude, with a marginally larger B_x —this observation is consistent with the time-averaged A_{\parallel} shown in Figure 5. The time traces of

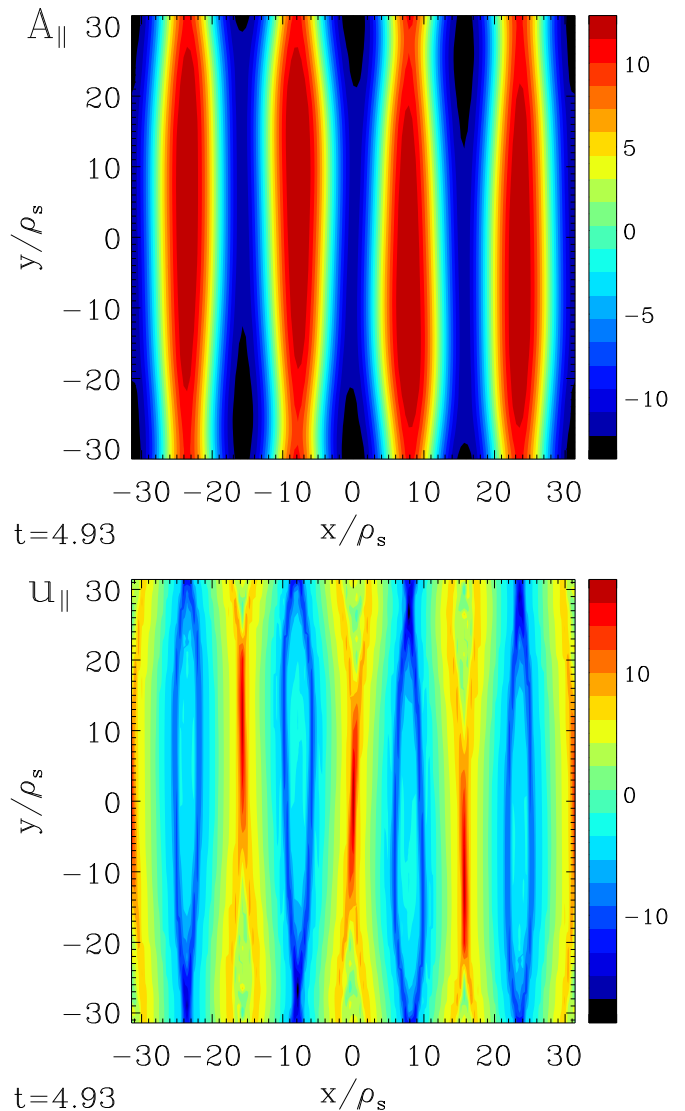


Figure 3. Contours of A_{\parallel} (above) and the parallel electron flow speed $u_{\parallel e}$ (below), the latter in units of $c_s \rho_s / L_{\text{ref}}$, at $t \approx 5$. At this point, the current sheet starts to break up, but turbulence has not yet developed. The electron flow speed is the dominant constituent of the perturbed plasma current (the other being the much smaller ion flow speed).

(A color version of this figure is available in the online journal.)

$B_{x,y}$ also illustrate that the dynamical or correlation time of the fluctuating fields is indeed much shorter than the collisional decay time τ_{decay} , as claimed in Section 3. Moreover, a clear quasi-stationary saturated state is achieved, as expected when net energy input from the drive term balances dissipation.

To understand the precise balance of the most important modes in the system, one may consult Figure 7. Here the temporal evolution of various mode numbers of $|A_{\parallel}|$ is shown for the early phase of the simulation. During the linear phase (again, $t \lesssim 10$), the aforementioned depletion of the current sheet at $(4, 0)$ —denoting $(k_x/k_{x,\text{min}}, k_y/k_{y,\text{min}})$ —is visible, while the linearly unstable modes $(0, 1)$, $(0, 2)$, and $(0, 3)$ are growing. Once the transition to the nonlinear phase is completed, an intermediate stage begins, which lasts approximately until $t \approx 70$; during which $(0, 2)$ still competes with $(0, 1)$, but the nonlinear forward cascade already transfers energy to the subdominant and stable modes. Once this transitional stage is completed, the system settles into the quasi-stationary state. The

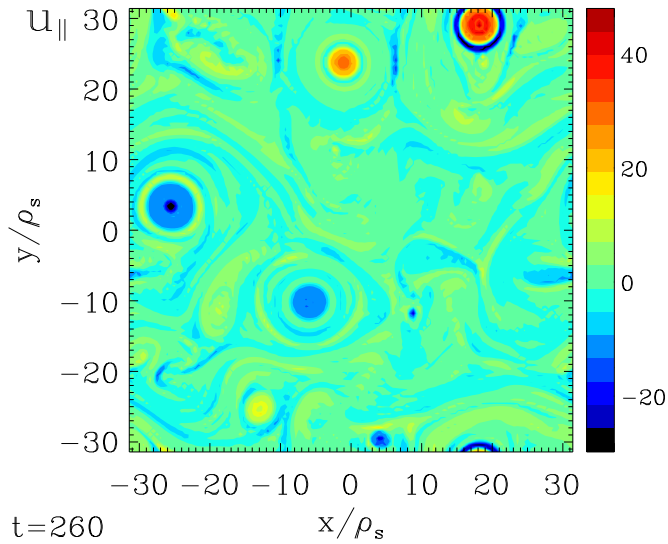
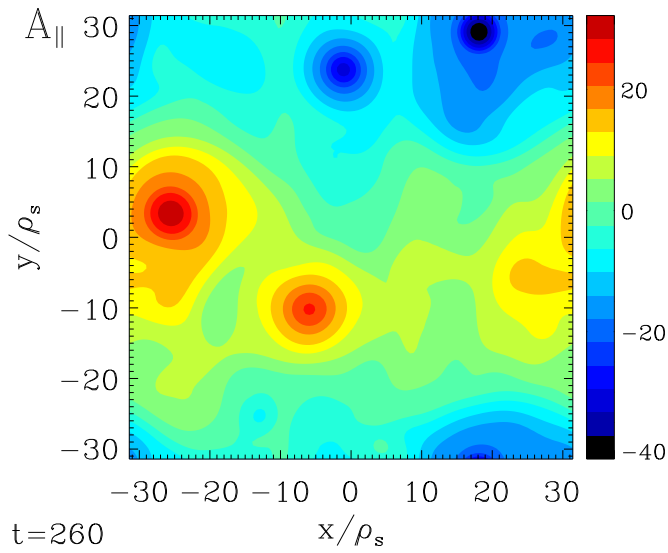


Figure 4. Contours of A_{\parallel} (above) and u_{\parallel} of the electrons (below), at $t = 260$. Now the system is fully turbulent, symmetry is broken, and the original current sheets are no longer visible; in their stead, plasmoids and current filaments dominate the appearance of $u_{\parallel e}$. Compare Figure 3.

(A color version of this figure is available in the online journal.)

dominant stable mode at $k_x = 0$ is $(0, 4)$, which is also included in the figure.

As one may expect intuitively, the saturation level of the $(4, 0)$ mode, relative to the initial value, depends on the nonlinear drive ω_{dr} . Larger values of ω_{dr} lead to larger saturated amplitudes of the current sheet mode, as the drive term is able to force the $k_y = 0$ mode back to the initial state more effectively.

These spectral properties are also reflected in the amplitude spectra of A_{\parallel} , which are shown alongside those of Φ , B_{\parallel} , and the perturbed electron density n_e in Figure 8. Here quadratic k_x and k_y spectra are shown. Technically, spectra of $k_{\perp} = (k_x^2 + k_y^2)^{1/2}$ may deviate, but it has been verified—independently of the curves shown in Figure 8—that, in particular, the slopes at higher $k_{x,y}$ are the same as those at the corresponding k_{\perp} . Hereafter, k_{\perp} is therefore used simply to refer to k_x and k_y equally.

Two spectral regions can be identified: At low k_{\perp} , the spectra of B_{\parallel} and n_e flatten out entirely, whereas Φ and A_{\parallel} are moderately steep, reflecting—particularly in the k_y spectra—the presence of the linearly unstable modes. At higher k_{\perp} , the

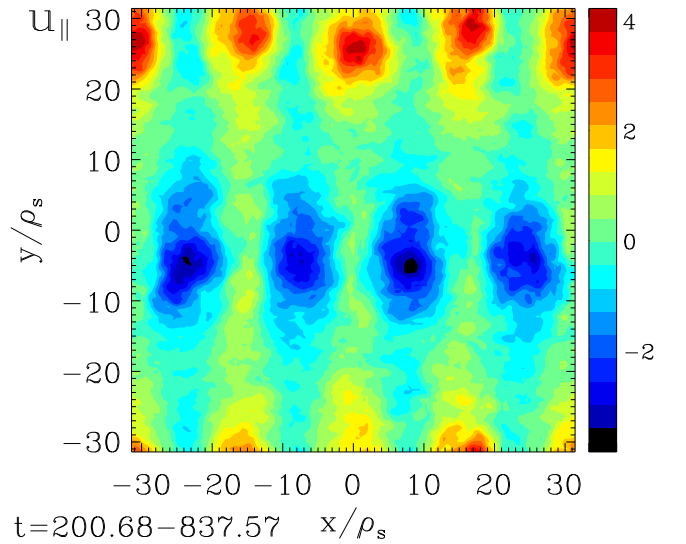
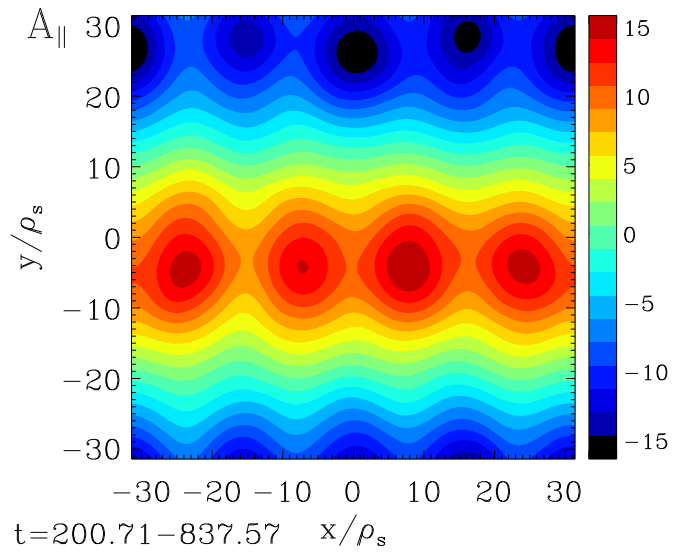


Figure 5. Contours of A_{\parallel} (above) and u_{\parallel} of the electrons (below), time-averaged over the quasi-stationary, saturated state. The influence of the current sheets is visible in $u_{\parallel e}$, whereas A_{\parallel} shows signs of an inverse cascade similar to decaying turbulence.

(A color version of this figure is available in the online journal.)

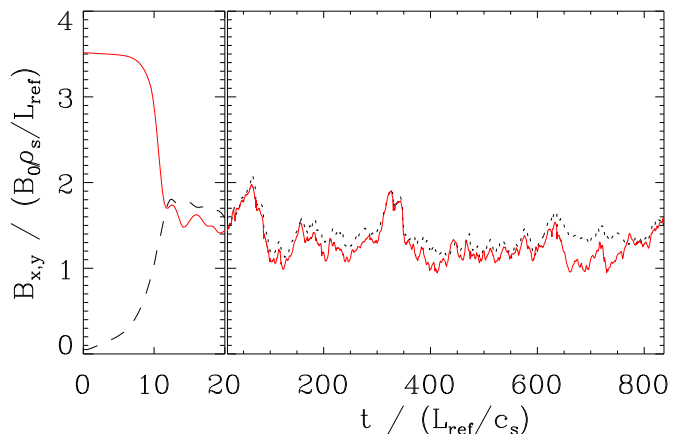


Figure 6. Magnetic field fluctuations B_x (black dashed line) and B_y (red solid line). During the magnified linear phase, isotropization occurs. During the saturated period, B_x slightly exceeds B_y on average, consistent with Figure 5.

(A color version of this figure is available in the online journal.)

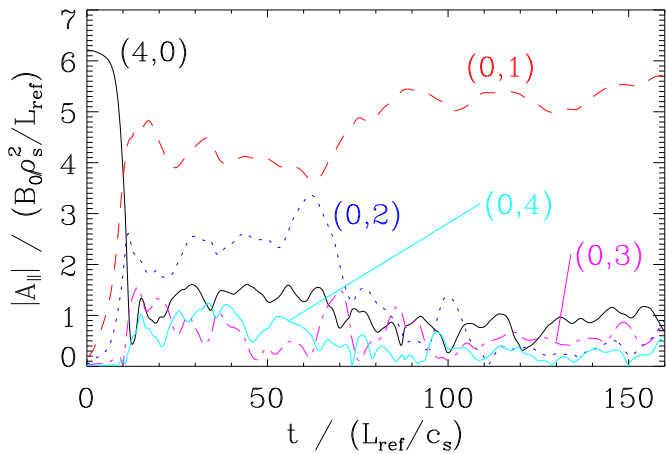


Figure 7. Absolute value of the fluctuating magnetic potential. Shown are the linear growth and early saturation phases for $A_{\parallel}(k_x/k_{x,\min}, k_y/k_{y,\min})$. In particular, (4, 0) corresponds to the current sheet, which is depleted significantly before the drive term can stabilize it; (0, 1–3) are the linearly unstable modes that grow (from varying initial amplitudes) until, eventually, (0, 1) dominates the quasi-stationary state; and (0, 4) is a characteristic example of a linearly stable mode, which only receives energy through the turbulent cascade.

(A color version of this figure is available in the online journal.)

picture becomes more isotropic, and the spectra for k_x and k_y are near-identical in this region. The spectral slopes in this quasi-inertial range (throughout which dissipation occurs, however) for $\langle \Phi^2 \rangle$ and $\langle A_{\parallel}^2 \rangle$ are -4 and -6 , respectively, corresponding to $E_{\perp} \sim k_{\perp} \Phi \propto k_{\perp}^{-1}$ and $B_{\perp} \sim k_{\perp} A_{\parallel} \propto k_{\perp}^{-2}$. This is of relevance to the parallel electric field and heating rate, which are introduced below.

These slopes agree with typical values for kinetic Alfvén wave (KAW) turbulence; see Howes et al. (2008), where a parallel antenna current was used for driving, or Boldyrev & Perez (2012), where large-scale forcing supplies energy. Taking from the former their definition for the magnetic energy $E_{B\perp} \sim k_{\perp}^3 A_{\parallel}^2$ and looking at the spectral slope in the range $1 < k_{\perp} \rho_s < 7$, one obtains $E_{B\perp} \propto k_{\perp}^{-2.7}$, while Figure 8 corresponds to a similar slope for $E_{B\perp}$ slightly shallower than k_{\perp}^{-3} . For comparison, solar wind observations yield slopes in the vicinity of $k_{\perp}^{-2.8}$ (Alexandrova et al. 2009; Chen et al. 2012), consistent with the aforementioned or the present numerical results. In general, KAWs propagate along the magnetic field. While ∂_z is zero in the present case, k_{\parallel} picks up a k_{\perp} contribution through the perturbed magnetic field; therefore, the observed similarities may stem from a KAW cascade at higher k_{\perp} with an oblique propagation angle. Further studies will have to reveal whether KAWs are indeed responsible for the slopes found in Figure 8.

After this discussion of the general properties of reconnection turbulence, the focus is now turned specifically to particle acceleration and heating due to parallel electric fields.

4.2. Parallel Electric Field and Heating Rate

Magnetic reconnection is known to cause particle acceleration through the formation of parallel electric fields (see, e.g., Neukirch 1996; Pritchett 2006). For the present purpose, the following definition is useful, dividing the parallel electric field into three components:

$$E_{\parallel} = E_{\parallel}^{\text{es}} + E_{\parallel}^{\text{fl}} + E_{\parallel}^{\text{ind}} = \frac{\partial \Phi}{\partial z} + \frac{\mathbf{B}_{\perp} \cdot \mathbf{E}_{\perp}}{B_0} - \frac{\partial A_{\parallel}}{\partial t}. \quad (7)$$

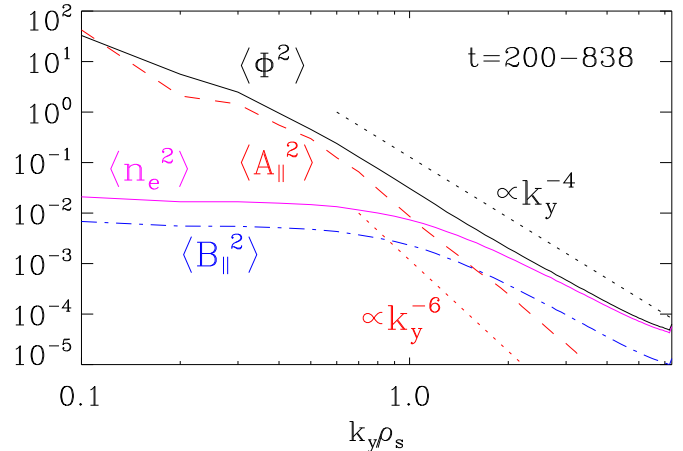
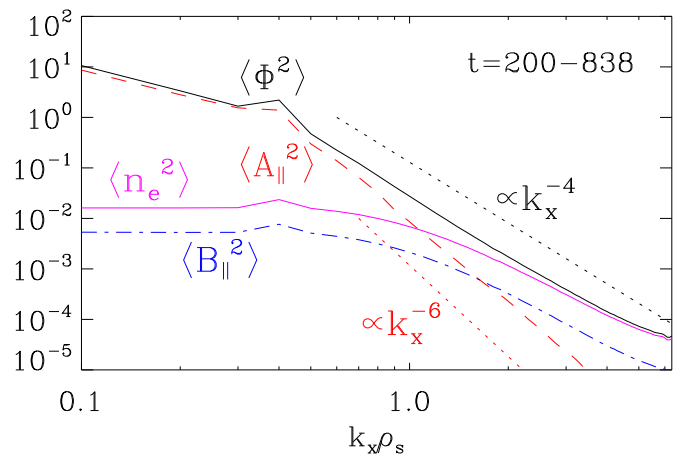


Figure 8. Spectra of the perturbed fields and electron density, as functions of k_x (above) and k_y (below). All quantities shown have the absolute square taken and are then averaged over the remaining wave number coordinate. For reference, slopes $\propto k^{-4}$ and $\propto k^{-6}$ are included as dotted black and red lines, respectively. The k_x and k_y spectra are mostly identical, with the exception of the drive range at low k_{\perp} , where the linearly unstable modes have higher amplitude in the k_y spectra.

(A color version of this figure is available in the online journal.)

Here $E_{\parallel}^{\text{es}}$ is the electrostatic contribution arising from a possible variation of Φ along the background magnetic field; by definition, this term is equal to zero in the present approach, which sets $\partial_z \rightarrow 0$. The term $E_{\parallel}^{\text{fl}}$ denotes the so-called flutter contribution—the perturbed magnetic field projects perpendicular electric field fluctuations along the unperturbed magnetic field (as in Rechester–Rosenbluth transport; Rechester & Rosenbluth 1978)—and $E_{\parallel}^{\text{ind}}$ is the inductive term, stemming from the temporal variation of the perturbed magnetic field. All these terms are normalized to $T_{e0} \rho_s / (e L_{\text{ref}}^2)$, where e is the elementary charge. Note that if the z coordinate was to be resolved in a fully three-dimensional simulation, its characteristic length scale would be $L_{\text{ref}} \gg \rho_s$, resulting in a $\partial_z \Phi$ that is of the same order as $E_{\parallel}^{\text{fl}}$ or $E_{\parallel}^{\text{ind}}$. It should be stressed that as there is no symmetry breaking along the parallel direction, i.e., E_{\parallel} has no preferred sign. Inclusion of $E_{\parallel}^{\text{fl}}$ is not universal in other works, but it will be demonstrated below that it is important, as the flutter consistently exceeds the inductive component.

The first plot in Figure 9 shows, as root mean squares, the time evolution of the total E_{\parallel} as well as the two nonzero constituents. The flutter contribution can be seen to account for almost the entire total electric field throughout almost the entire time range.

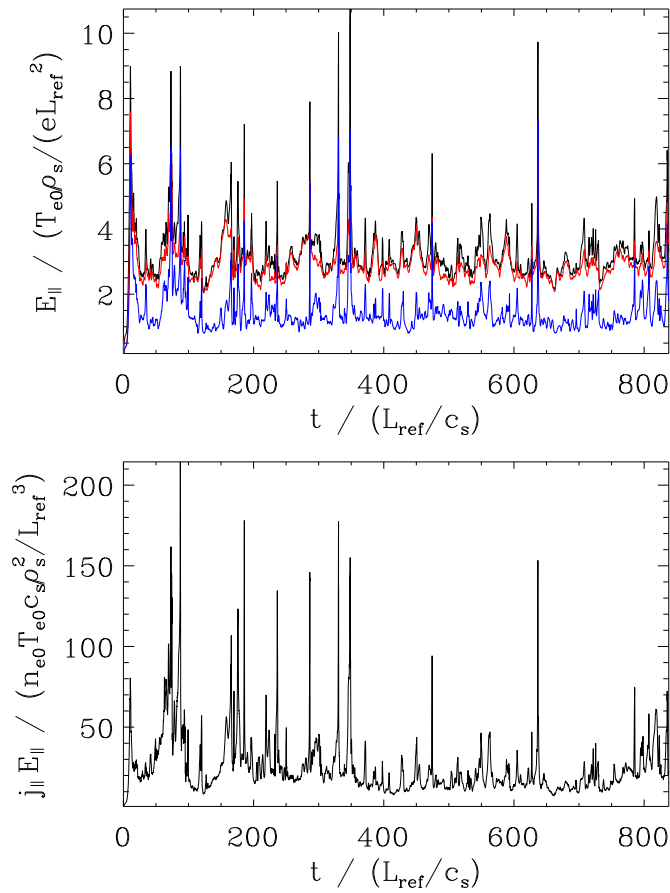


Figure 9. Time evolution of the parallel electric field (above) and the heating rate (below) for the standard parameter set. In the above plot, the three curves correspond to, from top to bottom: the total field (black), the flutter component (red), and the inductive component (blue); see the text. The heating rate $j_{\parallel} E_{\parallel}$ refers to heating due to kinetic particle acceleration rather than collisional dissipation. All quantities are obtained as root mean squares of the spatial domain.

(A color version of this figure is available in the online journal.)

As A_{\parallel} enters into both $E_{\parallel}^{\text{fl}}$ and $E_{\parallel}^{\text{ind}}$, it is not surprising that small fluctuations tend to occur simultaneously in both of these components; i.e., a spike in $E_{\parallel}^{\text{fl}}$ is mostly accompanied by a spike in $E_{\parallel}^{\text{ind}}$. The bigger spikes in particular are the result of mergers of plasmoids of the same sign in the current, an aspect of the turbulence that will be discussed below. Note that the only moments when $E_{\parallel}^{\text{fl}}$ and $E_{\parallel}^{\text{ind}}$ become comparable are during the biggest bursts. Even then, however, $E_{\parallel}^{\text{fl}}$ remains an important contributor to the total parallel electric field.

In the same figure, the second plot contains the (root mean square of the) heating rate, defined as

$$j_{\parallel} E_{\parallel} = (q_e u_{\parallel e} + q_i u_{\parallel i}) n_{e0} E_{\parallel}, \quad (8)$$

which has the units $n_{e0} T_{e0} c_s \rho_s^2 / L_{\text{ref}}^3$ (with $n_{i0} = n_{e0}$ due to quasineutrality). The quantity j_{\parallel} is the perturbed current along the magnetic field, carried mainly by the electrons. There are no lower-order terms to the heating rate due to the fact that there is no current or parallel electric field included in the equilibrium. Partially offsetting the fact that $j_{\parallel} E_{\parallel}$ contains a factor of L_{ref}^{-3} , its numerical values can be rather large, as visible in Figure 9 and even more so in very confined local regions in Figure 10. Thus, this form of heating may provide an efficient mechanism for particle acceleration. Alternatively, E_{\parallel} alone may be thought to

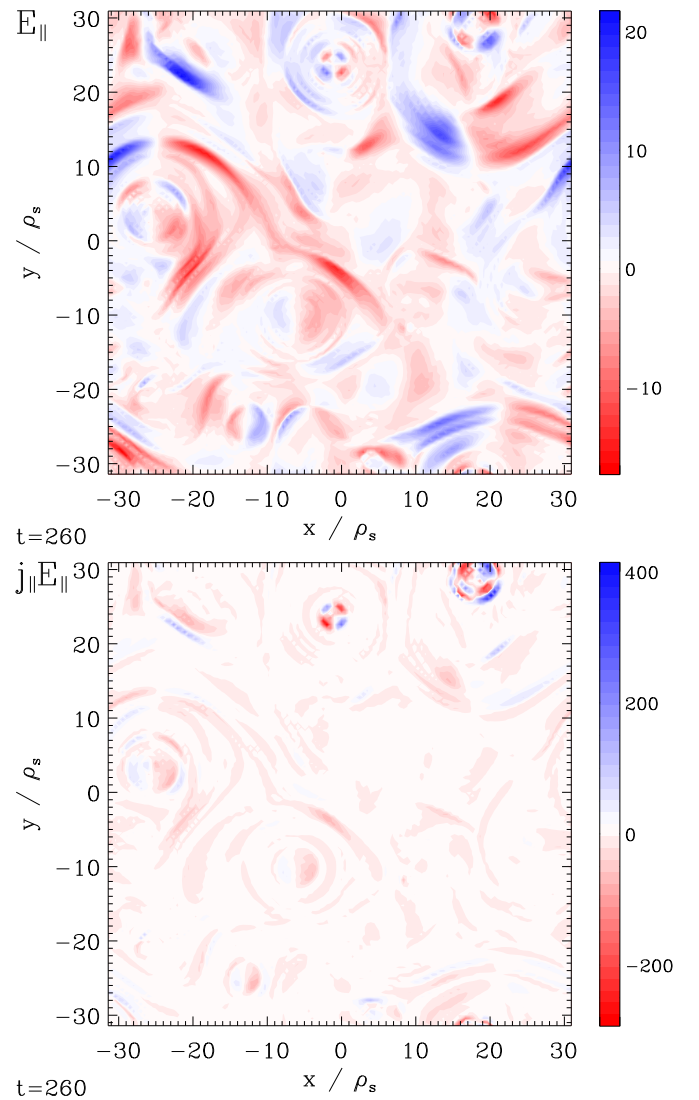


Figure 10. Contours of the parallel electric field (above) and the heating rate (below), taken from the same simulation and time step as the data shown in Figure 4. The more filamentary structure of the electric field is washed out when multiplied with the current, as both are particularly strong in locations where plasmoids exist.

(A color version of this figure is available in the online journal.)

provide a means of energizing test particles. To what degree $j_{\parallel} E_{\parallel}$ heating may be relevant to the solar corona is to be addressed in Section 6.

Heating as used throughout this work not only refers simply to a change in (perturbed) temperature but may also create or enhance non-Maxwellian components in the distributions. For comparisons with high-energy power-law tails in solar plasmas, one would have to drastically increase velocity space or, alternatively, include passive particle species with high background temperatures and observe their saturated state (as was done with the GENE code in Pueschel et al. 2012). Such simulations, however, come with a high computational price tag, since—aside from the need to compute the Vlasov equations for all new species—more restrictive constraints on the simulation time step arise. Separate efforts will therefore have to be undertaken to study this effect.

The spatial structure of E_{\parallel} comprises significant filamentation, along with ubiquitous quadrupole features; see Figure 10.

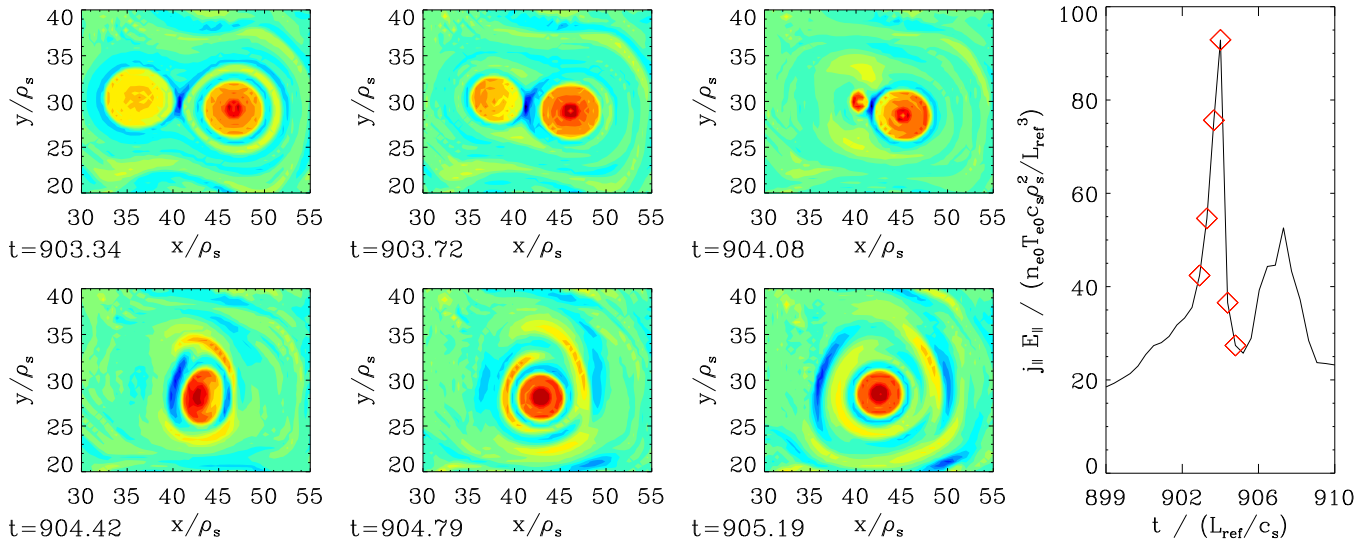


Figure 11. Merger of two plasmoids. Shown are contours of $u_{\parallel e}$ for various time steps, with the amplitudes in each plot normalized to the minimum and maximum over the entire x - y plane at that respective time. On the right, these time slices are marked as red diamonds on a time trace of the heating rate; clearly, the merger coincides with a strong spike in heating. Note that the second, smaller peak on the right corresponds to an unrelated merger event at a different location.

(A color version of this figure is available in the online journal.)

The latter stem from $E_{\parallel}^{\text{fl}} \propto B_x E_x + B_y E_y$, whereas the inductive component $E_{\parallel}^{\text{ind}}$ (not shown) tends to produce larger-scale structures similar in shape to A_{\parallel} . A few large-amplitude quadrupoles dominate the contours of the heating rate. These are strong plasmoids, simultaneously corresponding to locations of large circular parallel current regions and of quadrupoles in E_{\parallel} . When comparing with Figure 9, this also explains why the spikes associated with plasmoid mergers in $j_{\parallel} E_{\parallel}$ are much larger than in E_{\parallel} , relative to the ambient turbulence: the former depends much more strongly on the plasmoids than does the latter. These heating spikes and their underlying plasmoid mergers are addressed next.

4.3. Plasmoid Merger Events

Plasmoids form in the turbulence as soon as the initial current sheet breaks up. They are then able to float around in the x - y plane somewhat freely, but their statistical location is influenced moderately by the current sheet, as is evident from the time-averaged current structures in Figure 5. In many cases, the associated current produces multiple layered ringlike structures around the plasmoid core, often reversing sign when moving from one ring to the next, in effect partially shielding the plasmoid from others of its kind; this feature is not unlike Debye shielding in an electrostatic force picture. As parallel currents feel an attractive force, plasmoids of the same sign (or, in contour plots, of the same color) attract one another and may merge if they approach each other too closely—in fact, such merger events occur with great regularity. Conversely, opposite signs result in a repelling force.

Parker (1988) discusses the possibility of magnetic reconnection being the cause for spikes in X-ray intensities in the solar corona. Section 6 explores, among other things, whether said spikes may be related to the kind of plasmoid merger events so ubiquitous in the present simulations.

Figure 11 provides an example: Shown here is a portion of the perpendicular plane for six narrowly spaced moments in time (with 500 simulation time steps between adjacent time slices in the figure). Note that the perpendicular simulation box is the same as in previous figures, but values of x and y may

run higher than 10π due to the periodic boundary conditions. In the beginning (upper left), this region contains two well-sized plasmoids of positive sign (red), surrounded by rings of negative current (blue) that touch in one single location, marking the X point associated with this particular pair of plasmoids. As the plasmoids are attracting each other, the X point region is compressed until, eventually, the right plasmoid absorbs its left counterpart and becomes a new, single plasmoid (lower right). Further on the right, the heating rate for this short time window is plotted for comparison, with the time steps of the contours marked as red diamonds. It is evident from that plot that the merger event coincides perfectly with a strong spike in $j_{\parallel} E_{\parallel}$, which is not surprising since the sudden compression of the X point leads to high- k_{\perp} contributions in both A_{\parallel} and Φ , entering in an amplified manner into $E_{\parallel} \sim E_{\parallel}^{\text{fl}} \sim k^2 A_{\parallel} \Phi$. The case selected for this figure is very representative of other plasmoid mergers and heating spikes. While in some cases, a typical plasmoid may merge with a slightly more oblate structure, it is almost always possible to identify the merger event that brought about a strong rise of the heating rate.

While it requires significant computational resources to properly study the statistics of plasmoid mergers, a few central results are presented from a longer simulation at default parameters (from which the data in Figure 11 were taken). The following characteristics are thus obtained: Taking the heating rate for a time period of length 1606, one may define a spike to occur whenever $\langle j_{\parallel} E_{\parallel} \rangle_{\text{rms}}$ exceeds its time-averaged value (for this simulation, 22.6) by a factor of two. For the time period under investigation, this definition yields a total of 50 spikes, making the characteristic plasmoid merger separation timescale $\tau_{\text{merge}} = 32$; this number, however, can be expected to depend fundamentally on the perpendicular box size. Moreover, it is possible to measure the individual spike widths at a heating rate of twice the time average. Then averaging over all spikes, one arrives at a characteristic plasmoid merger duration of $t_{\text{merge}} = 2.06$. Coincidentally, the spike shown in Figure 11 has a very similar width. As before, all time-like quantities are normalized to L_{ref}/c_s . As the mergers are nothing but reconnection events, it can be speculated that the merger time is related to the linear tearing mode growth rate, with some correction

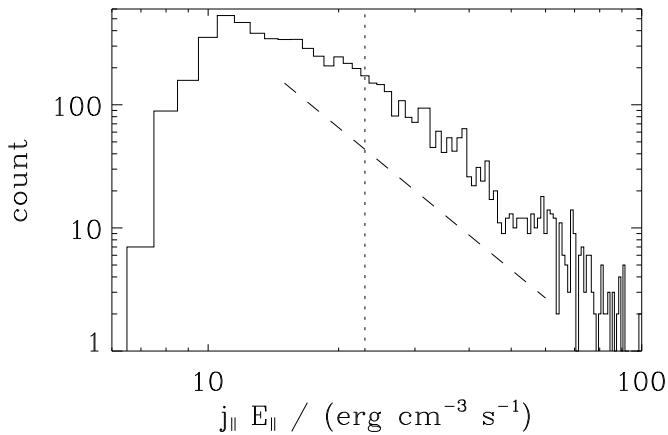


Figure 12. Histogram of $j_{\parallel} E_{\parallel}$ for default parameters, with bins shown only up to a value of 100; counted are individual time steps. The vertical dotted line denotes the point where half the integrated heating occurs at lower values and half at higher values. Bulk or background heating is to be found to the left of this line, whereas the strongest plasmoid merger bursts begin at the right end of the plot. A dashed line is included, corresponding to the best-fit power-law slope of -2.9 in that range of heating amplitudes. The histogram was created from the longest available simulation, covering a total time period of about 1600.

due to the plasmoid size relative to the current sheet width. In fact, t_{merge} is of the same order as γ^{-1} . Rigorously testing this hypothesis requires long time statistics of nonlinear runs for various other parameter settings and therefore has to be deferred to future work. Preliminary tests presented further below in this section indicate, however, that t_{merge} is less sensitive to certain input parameters than γ .

The statement that the tearing growth time γ^{-1} may be related to t_{merge} does not contradict the findings of Loureiro et al. (2007) and others who report large growth rates $\gamma \gg \gamma_A$ associated with the plasmoid instability. First, the aforementioned X point compression is able to strongly enhance reconnection rates (see also the linear $k_x \equiv k_{cs}$ scan in Pueschel et al. 2011), thus decoupling the k_{cs} dependencies of γ^{-1} and t_{merge} . Second, as the definition of t_{merge} relies on the root mean square of the heating, background heating may leave an imprint on its parameter scalings. Overall, it is therefore reasonable to assume that t_{merge} exhibits many linear tearing mode properties but also additional, nonlinear features that are more consistent with the generally accepted picture of the plasmoid instability. Note also that the relation $t_{\text{merge}} \sim \gamma^{-1}$ is likely not to be fulfilled generally when going to different parameter regimes.

Regarding the previous comment that the present parameters are squarely in the Hall regime, one may wonder whether the above findings would not hint at a plasmoid-dominated regime. In Figure 12, the heating distribution is shown for the default parameter set, with the adaptive time step having been taken into account. As is clear from the figure, somewhat less than half of the total heating can be attributed to the peak on the left, which includes roughly Gaussian-distributed, steady heating, whereas the non-Gaussian tail to the right of this peak stems from plasmoids and—at the highest heating rates—from plasmoid mergers. It is therefore appropriate, for the present regime, to expect significant impact from plasmoids, although it needs to be stressed that the mechanism by which plasmoids are produced here is different from the usual setups on which regime distinctions tend to be based.

Figure 12 is in line with the general picture that small, burstlike phenomena contribute comparably with the background heating: in the solar corona, the flare power-law index α

(Hudson 1991) is rather close to the critical value of 2 (see, e.g., Benz & Krucker 2002; Hannah et al. 2008), above which—particularly in the quiet solar corona—nanoflare events dominate the heating. Note that the power-law exponent of 2.9 shown in the plot cannot directly be compared with the aforementioned value of 2. The statements made here are simply that a power-law scaling exists at higher heating rates and that plasmoids are responsible for a large fraction of the total heating.

Merging plasmoids have been investigated in many publications. Uzdensky et al. (2010) and references therein provide additional information on this topic. Additional gyrokinetic studies of plasmoid mergers in strong guide fields, and their relation to results from the aforementioned references, are deferred to a separate publication. Returning to the overall heating and to parallel electric fields, the impact of variations in the input parameters is discussed next.

4.4. Parameter Dependencies

In order to understand how changes in the physical input variables affect the turbulence, a number of nonlinear scans about the default parameter set were undertaken. Due to the great computational expense associated with this investigation, which included additional convergence tests in a number of cases, the scans in m_e/m_i , T_{i0}/T_{e0} , and Δv_{\parallel} contain only three data points each. The following parameter ranges are covered: $0.005 \leq \omega_{\text{dr}} \leq 0.5$; $0.0005 \leq \nu_c \leq 0.5$; $0.05 \leq \beta \leq 0.5$; $0.01 \leq m_e/m_i \leq 0.1$; $0.1 \leq T_{i0}/T_{e0} \leq 1$; $0.1 \leq \Delta v_{\parallel} \leq 1$; and $0.04 \leq k_{cs} \leq 0.8$. The impact of varying those parameters on the parallel electric field and the heating rate are of particular importance, and their scaling with three central variables— ω_{dr} , k_{cs} , and ν_c —is presented in detail below, before scaling exponents for all of the above parameters are given. The selection of the first two of these three parameters is motivated by their importance to solar corona scalings; see Section 6.

As a primary motivation for this study is to gain the ability to scale the heating rate to corona-like physical conditions, it is helpful to state here how general or approximate the validity of such an exercise can be expected to be. While future work will have to directly verify such extrapolations, there is good reason to trust in the applicability of the results of this section: Only three parameters are expected to be able to elicit changes between physical regimes—the collisionality or Lundquist number, when moving from the present collisionless to a collisional regime; the drive frequency, when arriving at decaying turbulence in the limit of low drive; and the current sheet wave number, when entering a regime where finite Larmor radius effects become important (typically this occurs for $k_{\perp} \rho_s \gtrsim 1$). As shall be demonstrated in Section 6, coronal parameters lie well outside any such new regimes. Dependencies on other parameters, based in part on the linear scaling results in Pueschel et al. (2011), can be expected to be continuous, making a straightforward extrapolation possible.

Central to the turbulent dynamics is the nonlinear drive. Figure 13 demonstrates that both E_{\parallel} and the heating rate fundamentally depend on the drive strength, as measured by ω_{dr} . Qualitatively, this situation can be likened to a source term in Ohm's law: If energy is injected, it will contribute to heating. Here, however, the nonlinear form of the drive term makes for a somewhat more complicated energy source. Of great importance is the fact that throughout almost the entire range of studied drive frequencies, the scaling does not change (with the exception of slight steepening in $j_{\parallel} E_{\parallel}$ at very low drive), showing that quenching of the turbulence due to an all-dominant source term

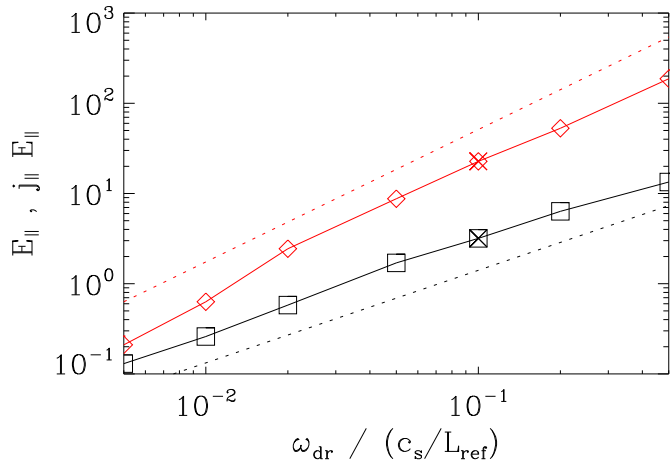


Figure 13. Scaling of E_{\parallel} (black squares) and the heating rate $j_{\parallel} E_{\parallel}$ (red diamonds)—in the usual normalized GENE units—with the nonlinear drive frequency ω_{dr} . The significant impact of ω_{dr} confirms that the drive term does not stifle the turbulence even as $\omega_{\text{dr}} \gtrsim \gamma$. Dotted lines show best-fit slopes; the corresponding numerical values are reported in Equations (9) and (10). For convenience, the results at default drive frequency have been marked with additional crosses.

(A color version of this figure is available in the online journal.)

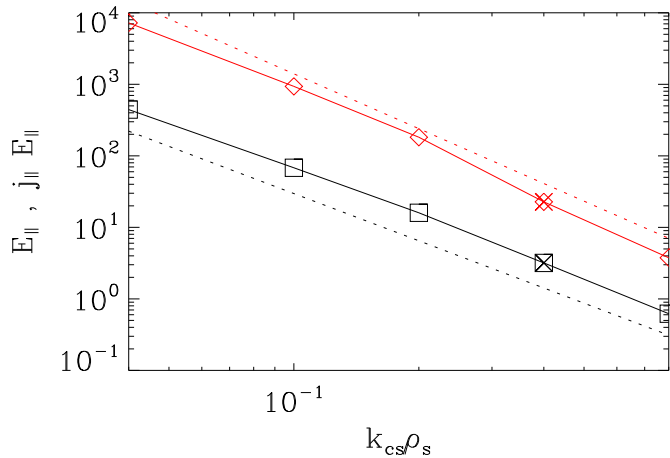


Figure 14. Scaling of E_{\parallel} (black squares) and $j_{\parallel} E_{\parallel}$ (red diamonds) with the wave number k_{cs} of the current sheet; see also the caption of Figure 13. Relatively steep dependencies are observed, which are partially offset by the k_{cs} dependence of B_{rec} , as discussed in Section 6.

(A color version of this figure is available in the online journal.)

does not occur, a consequence of the improved Krook drive compared with that in Pueschel et al. (2011).

The simulation with the lowest $\omega_{\text{dr}} = 0.005$ differs somewhat from those at higher drive frequencies; here the transition to decaying turbulence is setting in. Moreover, the nonlinear phase exhibits plasmoids in chainlike groups, with separate chains for plasmoids of positive current and negative current. As such, this case is more closely related to plasmoid chains studied, e.g., in Drake et al. (2006).

In Figure 14, the scalings of parallel electric field and heating rate with the driving wave number k_{cs} are shown. The dependencies are very stable over a wide range of k_{cs} values—this property aids in the accurate rescaling of these normalized results when applying them to solar plasma parameters. In particular, the values covered here all correspond to current sheet widths greater than ρ_s , allowing for straightforward extrapolation to larger scales, whereas one may expect finite-Larmor-radius effects to modify the scaling once $k_{\text{cs}} \gtrsim 2\pi$. Another feature,

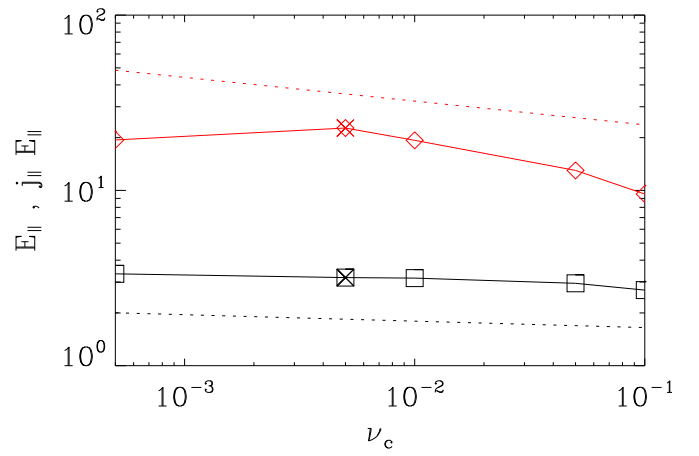


Figure 15. Scaling of E_{\parallel} (black squares) and $j_{\parallel} E_{\parallel}$ (red diamonds) with the collision frequency ν_c ; see also the caption of Figure 13. While the dependences seen here are relatively weak, a new regime begins to form at the highest collisionality. The ν_{cs} range of values shown here corresponds to a Lundquist number range of $3.3 \times 10^6 \geq S \geq 1.7 \times 10^4$.

(A color version of this figure is available in the online journal.)

however, is more surprising: the quantities plotted in Figure 14 decrease steeply as k_{cs} is increased, while linear growth rates of the tearing mode increase under the same circumstances (see Pueschel et al. 2011 and further down in this section). As both E_{\parallel} and $j_{\parallel} E_{\parallel}$ are comprised, in part, of structures smaller than the highest linearly unstable k_y mode (as presented in Figure 7) in the system, one might expect that the properties of E_{\parallel} and $j_{\parallel} E_{\parallel}$ would be influenced significantly by the cascade range of wave numbers. As shall be demonstrated below, however, using a quasilinear approach, these differences can be reconciled without relying on the nonlinear cascade.

The impact of collisionality on the kinetic heating, as opposed to its impact on the collisional dissipation, is the subject of Figure 15. Based on the linear tearing mode, one may expect the nonlinear system to be hardly influenced or weakly enhanced as the collisionality is increased. As is evident from the figure, very little dependence is observed; only at higher ν_c do the curves steepen somewhat, but at a negative slope—also compare Ng et al. (2012) at low resistivity. A similar regime change around $S \sim 10^4$ is recorded in Numata et al. (2011) for gyrokinetic simulations.

One can also draw parallels with the findings reported in Bhattacharjee et al. (2009) and Huang & Bhattacharjee (2010), where the reconnection time t_{rec} is found to be constant above a Lundquist number of $S \sim 10^5$, while the peak current density is decreasing with decreasing S near $S \sim 10^6$. Qualitatively, this agrees with the results shown in Figure 15, where E_{\parallel} (for which t_{rec} may be used as a proxy for this argument) is constant over a large range of S , whereas $j_{\parallel} E_{\parallel}$ is decreasing with ν_c near $S \sim 10^{-4}$ – 10^{-5} . This constitutes a slightly different range of values for S than that in Huang & Bhattacharjee (2010). Their arguments, however, are related to the plasmoid instability, the usual setup for which, as discussed previously, differs from the one used here. Similarly, Uzdensky et al. (2010) look at plasmoid chains to predict that the collisionality-independent regime starts near $S \sim 10^6$.

Additionally, the low- ν_c behavior is reminiscent of a recently observed feature of fusion-relevant microtearing modes, which are driven by the background electron temperature gradient: whereas previous work (Connor et al. 1990) had focused on a regime where microtearing modes are stabilized for low

collisionality, they become independent of v_c at $v_c \rightarrow 0$ and finite growth rate in another, new regime (Predebon & Sattin 2013; Carmody et al. 2013). In the former, the mode relies on the time-dependent thermal force, while in the latter, magnetic drifts lead to (radial) cross-field currents that destabilize a tearing mode, thus motivating this comparison.

In the context of wide-ranging parameter scans, an intuitive question is whether the prevalence of plasmoids conforms to the standard criterion (Biskamp 1986) on the Lundquist number for the plasmoid instability, namely that $S > S_{\text{crit}} \approx 10^4$. With the Lundquist numbers in Figure 15 covering $1.7 \times 10^4 \leq S \leq 3.3 \times 10^6$, and with plasmoids appearing for all these values, to determine whether the criterion is indeed consistent with the present observations, a look at lower S is instructive. It was stated in Section 2 that the lowest Lundquist number investigated here was below $S = 10^4$. In fact, one additional value was simulated, at $v_c = 0.5$, corresponding to $S = 3.3 \times 10^3$. At this point, localized high-amplitude noise of numerical origin at small scales appeared with regularity, utterly dominating the root mean square results. Focusing on regions without such noise (which tends to be fairly localized in the x - y plane), it is possible to ascertain a previous claim, however: consistent with the plasmoid criterion $S \gtrsim 10^4$, filaments have now become more prominent than circular structures in the turbulence.

In addition to the scalings shown in Figures 13–15, the remaining parameter dependencies are measured. Combining all results, one may write the parallel electric field (in the usual normalized units $T_{e0}\rho_s/(eL_{\text{ref}}^2)$) as

$$E_{\parallel} = 3.18 \left(\frac{\omega_{\text{dr}}}{0.1}\right)^{1.0} \left(\frac{v_c}{0.005}\right)^{0.0} \left(\frac{\beta}{0.5}\right)^{1.1} \times \left(\frac{m_e/m_i}{0.01}\right)^{-0.5} \left(\frac{T_{i0}/T_{e0}}{1.0}\right)^{0.0} \left(\frac{\Delta v_{\parallel}}{0.5}\right)^{1.1} \left(\frac{k_{\text{cs}}}{0.4}\right)^{-2.2} \quad (9)$$

and, similarly, the heating rate (as before, in units of $n_{e0}T_{e0}c_s\rho_s^2/L_{\text{ref}}^3$) as

$$j_{\parallel}E_{\parallel} = 22.7 \left(\frac{\omega_{\text{dr}}}{0.1}\right)^{1.5} \left(\frac{v_c}{0.005}\right)^{-0.1} \left(\frac{\beta}{0.5}\right)^{1.3} \times \left(\frac{m_e/m_i}{0.01}\right)^{-1.1} \left(\frac{T_{i0}/T_{e0}}{1.0}\right)^{0.0} \left(\frac{\Delta v_{\parallel}}{0.5}\right)^{1.8} \left(\frac{k_{\text{cs}}}{0.4}\right)^{-2.55} \quad (10)$$

Regarding the exponents in the above equations, an error of ± 0.1 is characteristic for the accuracy of the fits; only for the v_c scan is there a region observed where a power-law fit starts to break down (see Figure 15), with perhaps another breakdown to be expected at even lower ω_{dr} than those studied here. While technically these expressions have been derived in the vicinity of the default parameter set, they can also be used to obtain predictions for parameters not achievable in present-day simulations. It will be useful for future studies to extend certain scans, for instance in the case of collisionality, to push into other parameter regimes.

It is important to understand to what degree linear tearing is able to predict these scalings. Not taking into account the purely nonlinear parameter ω_{dr} , the linear parameter dependencies—again, with γ in units of c_s/L_{ref} —tend to deviate somewhat

from those in Equations (9) and (10):

$$\gamma = 0.156 \left(\frac{v_c}{0.005}\right)^{0.1} \left(\frac{\beta}{0.5}\right)^{0.0} \left(\frac{m_e/m_i}{0.01}\right)^{-0.15} \times \left(\frac{T_{i0}/T_{e0}}{1.0}\right)^{0.0} \left(\frac{\Delta v_{\parallel}}{0.5}\right)^{1.0} \left(\frac{k_{\text{cs}}}{0.4}\right)^{1.1} \quad (11)$$

Not surprisingly, considering the similar parameter set used there, the above exponents agree rather well with the results of the dependency studies in Pueschel et al. (2011).

The growth rates in Equation (11) were taken at $k_y = 0.1$, which, based on Figure 7, is expected to outweigh the other linearly unstable modes in the nonlinear simulations. A simple means of comparing the linear scalings with their nonlinear equivalents is by forming a quasilinear fraction γ/k_{\perp}^2 and then doubling and tripling the scaling exponents to arrive at predictions for E_{\parallel} and $j_{\parallel}E_{\parallel}$, respectively. Simply taking $k_{\perp} \sim k_{\text{cs}}$ leads to the following quadratic quasilinear scalings: $Q \propto v_c^{0.2}\beta^{0.0}(m_e/m_i)^{-0.3}(T_i/T_e)^{0.0}\Delta v_{\parallel}^{2.0}k_{\text{cs}}^{-1.8}$, which can be compared directly with Equation (9). Moderate differences exist in the parallel velocity shift dependency, whereas the collision frequency, the temperature ratio, the mass ratio, and the current sheet wave number are described relatively well by the linear predictions. The biggest outlier is the exponent of β : the linear simulations indicate essentially no impact on γ , whereas the nonlinear results correspond to a near-linear dependence. This, however, is not surprising: E_{\parallel} is dominated by its flutter component, which contains a factor $\mathbf{B}_{\perp} \propto A_{\parallel} \propto \beta$. Therefore, if $\gamma \propto \beta^0$, the intuitive prediction for the nonlinear case becomes $E_{\parallel} \propto \beta^1$, very close to the exponent in Equation (9). While there clearly is no perfect agreement between linear and nonlinear results, the values are still reasonably similar in most cases; it would appear that the linearly unstable region causes a strong imprint of physics onto the turbulent system, with the cascade at higher k_{\perp} adding additional and possibly deviating behavior that is not described by linear tearing mode physics.

As mentioned previously, obtaining good scaling relations for the plasmoid merger timescales t_{merge} and τ_{merge} would require significantly extending most of the simulations performed for these scans. While extracting a well-converged saturation level tends to be possible with a simulation covering only a few hundred time units, mergers sufficient in number for statistical analysis tend to occur over a time period of $\mathcal{O}(1000)$ or more. Therefore, only a cursory analysis is possible with the present simulation data; it suggests that t_{merge} depends at most rather weakly on the input parameters. In fact, taking into account the poor statistics for this case, the situation is consistent with there being no dependence of t_{merge} on any of the input variables; if there are any exceptions, the most likely candidates are ω_{dr} , Δv_{\parallel} , and perhaps k_{cs} , where scaling exponents may be as steep as -0.5 . A more thorough investigation along these lines has to be deferred to future work.

A variety of analyses has been presented relating to kinetic heating as a consequence of particle acceleration by parallel electric fields. Another means of heating is provided by collisions, through direct collisional dissipation. This topic is covered next.

4.5. Collisional Heating

For the standard set of parameters, the collision rate is comparable to the peak of the linear growth rate when expressed in the same units. In many cases, this hints at a semi-collisional

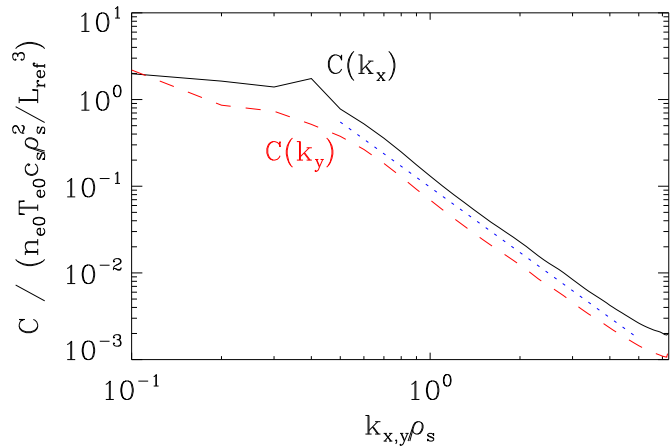


Figure 16. Collisionally induced energy dissipation $C = dE/dt|_{\text{coll}}$ as function of k_x (black solid line) and k_y (red dashed line). In the wave number range [0.5, 5], a blue dotted straight line $\propto k^{-2.5}$ is shown for reference.

(A color version of this figure is available in the online journal.)

regime. This rule has been shown not to be applicable, with the prior findings on turbulence scalings indicating that the system is more than one order of magnitude in v_c away from experiencing any sizable impact from collisions. Separate from how collisions affect the turbulent dynamics, however, is the question of whether they are able to cause appreciable heating. To quantify the collisional heating, direct measurements in the simulation data are thus conducted.

The gyrokinetic free energy has been discussed, e.g., in Bañón Navarro et al. (2011a), Bañón Navarro et al. (2011b), and Plunk et al. (2012). Here the definition

$$E(k_x, k_y) = \sum_j \int dv_{\parallel} d\mu \frac{T_{j0}}{F_{j0}} \left(g_j(k_x, k_y) + q_j \frac{F_{j0}}{T_{j0}} \chi_j(k_x, k_y) \right)^* \times g_j(k_x, k_y) \quad (12)$$

is used (Pueschel et al. 2013). Note that here and in the following, the term *energy* technically refers to an energy density. While, in general, various terms may affect the time evolution of the energy, the present focus lies on the impact of the collision term in the Vlasov equation, Equation (2). Defining $C \equiv dE/dt|_{\text{coll}}$ to be the collision-induced rate-of-change of the gyrokinetic free energy, it is possible to measure this impact during a simulation directly, yielding a time average of $\langle C \rangle_{\text{rms}} = 0.41$, in units of $n_{e0} T_{e0} c_s \rho_s^2 / L_{\text{ref}}^3$. This value can be compared directly to the kinetic heating rate $j_{\parallel} E_{\parallel}$, which evaluates to 22.7 for these parameters, clearly showing that kinetic far outpaces collisional heating. However, two additional findings may be gleaned from this analysis.

First, since $\partial f / \partial t|_{\text{coll}} \propto v_c$, it follows that $C \propto v_c$, as long as no new, collisional regime has been entered. Therefore, collisional heating is likely to surpass kinetic heating at around $v_c \approx 0.3$, very much in line with the threshold for the collisional regime discussed earlier.

Second, even though C is relatively small at $v_c = 0.005$, its spatial properties can be compared with results from other publications. Spectra of C in k_x (black solid line) and k_y (red dashed line) are shown in Figure 16. Much like in the case of the amplitude spectra in Figure 8, the two differ in the low- k_{\perp} range but become isotropic in slope almost as soon as the linearly stable range is reached. At higher $k_{x,y}$, both curves very closely follow the blue dotted line, which indicates a slope

of $k^{-2.5}$. This value agrees well with the Ohmic heating rate shown in TenBarge & Howes (2013). There a different setup is created to drive three-dimensional Alfvénic turbulence through a parallel antenna current. However, as in the present case, the drive is confined to the low- k_{\perp} region, and collision-induced dissipation is small compared with the predominant heating processes; therefore, a comparison between the high- k_{\perp} ranges of both approaches is indeed meaningful. It should be pointed out that their high-wave-number regime, normalized to ρ_s , spans roughly values from 30 to 100 (which is where the slope was measured for the above comparison), but at hydrogen mass ratio.

Having investigated in some detail the heating properties of the present form of reconnection turbulence, a new topic is broached next: the formation of temperature anisotropy, which also constitutes a recipient of energy via kinetic heating processes.

5. TEMPERATURE ANISOTROPY

In a magnetized plasma that is not fully dominated by collisional processes, temperature fluctuations parallel and perpendicular to the background field may develop independently to a certain degree. Various studies have focused on the effects of background temperature anisotropy on magnetic reconnection (Chen et al. 1984; Burkhart & Chen 1989; Tu & Marsch 2001; Matsui & Daughton 2008), while it has been claimed that guide field reconnection is not able to produce temperature anisotropy (Karimabadi et al. 2005). As shall be demonstrated here, however, tearing modes may indeed cause such anisotropy. This is of particular importance since ions in the solar wind exhibit anisotropic temperatures (Marsch et al. 1982; Kohl et al. 1997, 1998), with the corona the likely point of origin of said property; typically, cyclotron resonances are invoked in its explanation (Hollweg & Isenberg 2002), but the possibility of creating anisotropic temperatures in the absence of these resonances shall be investigated here. On a side note, Section 4 variously refers to isotropic features at high k_{\perp} ; this, however, is entirely unrelated to temperature isotropy as defined here.

In GENE, the perturbed distribution function is time evolved while the background distribution is in equilibrium, with $f_j \ll F_{j0}$. The temperature fluctuation $T_j \ll T_{j0}$ (which is an energy-like quantity) is not simply the second velocity moment of the perturbed distribution but contains another term, generally of the same order, that involves the perturbed density. Separating the components parallel and perpendicular to the background field, the following definitions apply (Görler 2009):

$$T_{\parallel j} = \frac{2\mathcal{M}_{20} - T_{j0}\mathcal{M}_{00}}{n_{j0}}, \quad (13)$$

$$T_{\perp j} = \frac{\mathcal{M}_{02} - T_{j0}\mathcal{M}_{00}}{n_{j0}}. \quad (14)$$

Here \mathcal{M}_{ab} denotes the $v_{\parallel}^a v_{\perp}^b$ velocity moment of the perturbed distribution, with $\mathcal{M}_{00} \equiv n_j$. First, with these definitions, the total temperature perturbation becomes $T_j = T_{\parallel j}/3 + 2T_{\perp j}/3$. Second, a Maxwellian velocity space in f_j at the same temperature as the background distribution causes the temperature fluctuation to vanish, as the \mathcal{M}_{00} term cancels the other moments in the above definitions.

This is true for the perpendicular temperature at the very beginning of the simulation, as observed in Figure 17 for the ions. The initialized current sheet, on the other hand, enhances

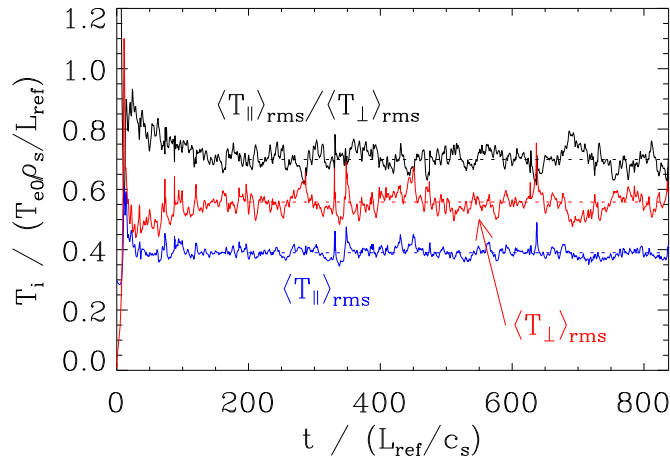


Figure 17. Parallel (blue) and perpendicular (red) ion temperature fluctuations as functions of time, in conjunction with the anisotropy factor (black) defined as the ratio of the two. At $t = 0$, the values are $\langle T_{\parallel i} \rangle_{\text{rms}} = 0.297$ (reflecting the ion contribution to the initial current sheet) and $\langle T_{\perp i} \rangle_{\text{rms}} = 0.007$ (a nonzero value due to the perturbation $\delta n_1 \ll n_1$). As the turbulence saturates, averaged levels (dotted lines starting at $t = 200$) can be extracted, corresponding to an anisotropy of $\mathcal{T}_i^{\text{ani}} = 0.699$.

(A color version of this figure is available in the online journal.)

\mathcal{M}_{20} and thus yields a finite T_{\parallel} . Almost as soon as the linear mode starts to grow, however, both temperature fluctuations increase at different rates (favoring T_{\perp}), until eventually they saturate at an anisotropy of $\mathcal{T}_i^{\text{ani}} = 0.699$ for default parameters. Here the definition

$$\mathcal{T}_j^{\text{ani}} = \frac{\langle T_{\parallel j} \rangle_{\text{rms}}}{\langle T_{\perp j} \rangle_{\text{rms}}} \quad (15)$$

has been used, where, in the above example, both constituents are far away from a zero fluctuation level, an important criterion to make this definition useful. To allow for alternative interpretations, another quantity is introduced, based on the velocity space moments directly:

$$\mathcal{V}_j^{\text{ani}} = \frac{\langle \mathcal{M}_{20,j} \rangle_{\text{rms}}}{\langle \mathcal{M}_{02,j} \rangle_{\text{rms}}} \quad (16)$$

Employing only the velocity moments of f_j , this definition compares the parallel and perpendicular temperatures of only the density perturbation n_j , whereas Equation (15) compares the full parallel and perpendicular temperature fluctuations of the system. While the standard definition is useful for a variety of purposes, some of the following analyses also include results obtained for the alternative form, for the reader's convenience.

Before providing additional details on the corresponding measurements in nonlinear simulations, it is instructive to briefly look at anisotropies of the linear tearing mode. Figure 18 contains $\mathcal{T}_j^{\text{ani}}$ as functions of k_y (black and red lines). While the ions significantly favor perpendicular temperature (with $\mathcal{T}_i^{\text{ani}} < 1$) throughout the entire range of wave numbers, the electrons have a mostly parallel temperature at low k_y , but reverse that property as higher k_y are reached. It is to be stressed that any initial anisotropy in the perturbed distributions f_j (the background distributions F_{j0} are isotropic by definition) stems solely from the presence of the current sheet at $k_y = 0$; the fact that the ions later favor T_{\perp} shows that the current sheet cannot be the source of their quasilinear or nonlinear anisotropy.

One other feature of Figure 18 warrants attention, captured by the dotted lines: the absence of collisions measurably alters the

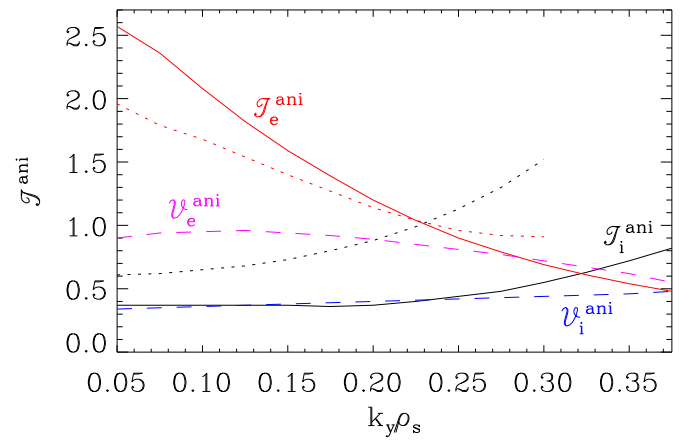


Figure 18. Temperature anisotropies for the linear tearing mode at default parameters. Shown as solid lines is the standard definition \mathcal{T}^{ani} from Equation (15) for ions in black and electrons in red and as dashed lines the moment-based definition \mathcal{V}^{ani} from Equation (16) for ions in blue and electrons in pink. The current sheet, which exists only at $k_y = 0$, does not factor into these results. Dotted lines correspond to \mathcal{T}^{ani} data from a collisionless simulation.

(A color version of this figure is available in the online journal.)

Table 1
Temperature Anisotropy

	QL	NL	NL _{k>}
$\mathcal{T}_i^{\text{ani}}$	0.43	0.70	0.81
$\mathcal{T}_e^{\text{ani}}$	1.40	2.92	3.57
$\mathcal{V}_e^{\text{ani}}$	0.40	0.43	0.31
$\mathcal{V}_i^{\text{ani}}$	0.86	0.53	0.76

Note. Anisotropies for ions/electrons, quasilinear/nonlinear (QL/NL) simulations, and using definitions $\mathcal{T}_j^{\text{ani}}$ (see Equation (15)) and $\mathcal{V}_j^{\text{ani}}$ (see Equation (16)). One additional column, labeled NL_{k>}, was evaluated using the nonlinear data only at $k_x > 0.5$, $k_y > 0.5$, which lies outside the linearly unstable region and instead represents the nonlinear cascade region of wave numbers.

anisotropy—lower k_y see a more isotropic mode relative to the case with finite v_c , whereas the ions gain parallel temperature at higher k_y as v_c is set to zero. This appears counterintuitive, as collisions are expected to isotropize the plasma. On the other hand, given that $v_{ei} \sim \gamma$, finite collisionality may affect the linear drive; compare collisional enhancement of collisionless tearing in Porcelli (1991). Also consider that the ions are less likely than the electrons to be subject to strong isotropization at moderate collisionalities.

Taking the linear values and weighting them with the growth rates from Figure 1, one obtains averaged, quasilinear anisotropies. Quasilinear estimates can be used to predict the properties of a (weakly) nonlinear system if the nonlinear property under investigation is governed solely by the linear physics. A very illuminating aspect of quasilinear tearing mode anisotropy, however, is that $\mathcal{T}_j^{\text{ani}}$ depends on Δv_{\parallel} (not shown in the figure). As a reminder: When expressing the linear growth rate in inverse Alfvén times, it is invariant under changes in Δv_{\parallel} , which only affect $\gamma [c_s / L_{\text{ref}}]$. If, even for the collisionless case, $\mathcal{T}_j^{\text{ani}}$ is sensitive to Δv_{\parallel} , theories based on Alfvénic normalization may not capture this effect.

In Table 1, all anisotropies for standard parameters are summarized: in addition to the quasilinear and nonlinear values, the last column contains nonlinear results when excluding the low- k_{\perp} range, to illustrate the impact of the nonlinear cascade (see also Cranmer et al. 2007 for a discussion of anisotropy in the turbulent cascade in fluid simulations). For the ions, see $\mathcal{T}_i^{\text{ani}}$ in

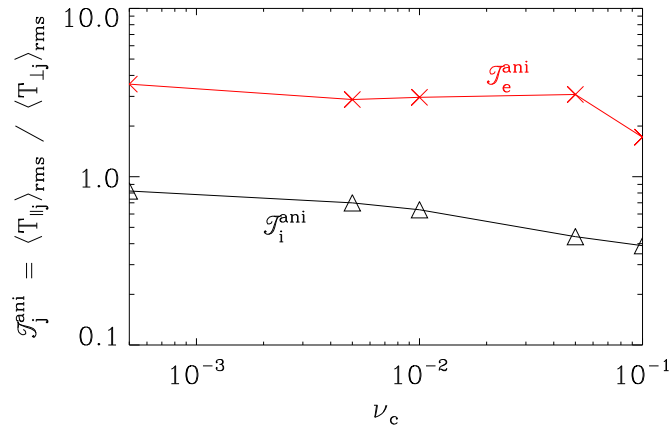


Figure 19. Temperature anisotropies as functions of the collision frequency ν_c : shown as black triangles is the ion anisotropy, while that of the electrons is marked by red crosses. For this figure, only the regular definition in Equation (15) is included. See also Figure 15, where E_{\parallel} and $j_{\parallel}E_{\parallel}$ are shown as functions of ν_c .

(A color version of this figure is available in the online journal.)

the table, the picture is consistent with an intuitive interpretation that the linear tearing mode causes anisotropy (favoring perpendicular temperature), which manifests itself mostly in the linearly unstable region but also, if only very moderately, reaches smaller scales through the cascade. The situation appears to be more complicated where the electrons and $\mathcal{T}_e^{\text{ani}}$ are concerned; here the anisotropy (consistently favoring parallel temperature) is increased from quasilinear to nonlinear to high- k_{\perp} nonlinear. Clearly, a cascade-range source of electron anisotropy exists, very possibly related to plasmoid mergers and heating bursts that involve higher k_{\perp} . Additional studies will have to be undertaken to illuminate the full physical picture of how the tearing mode creates—and how the turbulence moderates (for the ions) or enhances (for the electrons)—these anisotropies. Suffice to state here that the anisotropy is statistically related with $j_{\parallel}E_{\parallel}$ heating, although the picture is somewhat complicated by large fluctuations as well as the fact that kinetic heating impacts both T_{\parallel} and T_{\perp} .

As a side note, (electron) temperature anisotropy can be responsible for the excitation of the firehose and mirror instabilities (Bale et al. 2009). In the present case, temperature fluctuations are on top of a much larger background temperature $T_{j0} \sim T_j L_{\text{ref}}/\rho_s$, which is isotropic. However, one may envision a secondary process where the temperature of the density fluctuation would be prone to anisotropy-based instabilities; in that case, $\mathcal{V}_e^{\text{ani}}$ would be the quantity governing stability. Since $\beta < 1$, it is therefore concluded, given the anisotropies in Table 1 and Figure 18, that the firehose and mirror instabilities cannot be excited.

As an extension to the parameter scans presented in Section 4, the dependence of the temperature anisotropies on ν_c has been studied, with the results shown in Figure 19. They raise an interesting question: Why does the ion temperature anisotropy (black triangles), unlike that of the electrons (red crosses), undergo an enhancement (i.e., reach even lower values while already below 1) as ν_c is increased? First, electrons are more susceptible to the isotropization effect of collisions. This is confirmed by the sudden drop of $\mathcal{T}_e^{\text{ani}}$ at the highest ν_c in the figure, where a new collisionality regime starts to set in (see Section 4), whereas the ion curve sees no sudden changes at that point. Second, $\mathcal{T}_i^{\text{ani}}$ is related to quasilinear physics to a certain

Table 2
Physical Parameters for the Solar Corona

n_{e0}	B_0	B_{rec}
10^9 cm^{-3}	100 G	5 G
L_{ref}	ρ_s	ν_{ei}
10^9 cm	9.5 cm	87 s^{-1}
β	$T_{e0} = T_{i0}$	m_e/m_i
3.5×10^{-4}	10^6 K	1/1836

Notes. A fully ionized hydrogen plasma is assumed. The values shown here are taken from Cassak et al. (2006) and Priest & Forbes (2002). For these parameters, the ion sound speed evaluates to $c_s = 9.1 \times 10^6 \text{ cm s}^{-1}$.

degree: as the linear tearing mode experiences the influence of moderate collisionalities (compare Figure 18), it is able to increase its anisotropy. However, at a sufficiently large ν_c , this trend will reverse—until, eventually, $\mathcal{T}_i^{\text{ani}} = \mathcal{T}_e^{\text{ani}} = 1$, meaning both species will have perfectly isotropic temperatures once the physics are fully dominated by collisions.

As a last comment on temperature anisotropy, the turbulence simulation with $\Delta v_{\parallel} = 0.1$ has $\mathcal{T}_i^{\text{ani}} = 0.55$ and $\mathcal{T}_e^{\text{ani}} = 4.72$. The electrons are thus significantly more anisotropic than at default parameters, whereas the ion value has changed only slightly; this goes to show that quasilinear anisotropy (whose changes with Δv_{\parallel} are far weaker) does not capture the entire behavior of the nonlinear case, particularly for the electrons, which may experience effective parallel heating from plasmoids and plasmoids mergers.

6. APPLICATION TO THE SOLAR CORONA

It is instructive to revisit select results, particularly from Section 4, to apply them quantitatively to the conditions in the solar corona. To this end, physical parameters characteristic of fully ionized hydrogen, reconnecting solar corona plasmas (Cassak et al. 2006; Priest & Forbes 2002) are listed in Table 2. In the present section, all quantities are specified in cgs units. Note that considering significant currents are necessary to create a B_{rec} as specified in the table, it is intuitive to look at the instability threshold for ion acoustic waves, even though these waves are generally stable in the corona due to Landau damping. Using the results of Vranjes et al. (2009), the scale disparity between ρ_s and L_{ref} , which affects the perturbed electron density, invariably lowers the electron flow velocity below the critical value.

Considering the content of Table 2, two important input parameters are thus left to be determined. First, the current sheet replenishing timescale $\tau_{\text{repl}} = \omega_{\text{dr}}^{-1}$. As a starting point, in the absence of direct measurements, the default value from the previous sections is retained, with $\tau_{\text{repl}} = 10L_{\text{ref}}/c_s = 1100 \text{ s}$. This value lies above the characteristic timescale of about 10^2 s for microflares (Parker 1988) but below typical loop lifetimes on the order of 10^4 s (Winebarger et al. 2003; López Fuentes et al. 2007), whereas it agrees fairly well with typical turnover times of solar granules of ~ 10 minutes (Mehltretter 1978; Hirzberger et al. 1999), which may be thought of as the source location of energy injected into the current sheets. Second, the current sheet width $\lambda_{\text{cs}} = 2\pi/k_{\text{cs}}$. Available observational data are strongly limited by spatial resolution, with the smallest observable structures occurring at around 10^7 cm (Scharmer et al. 2008; Brooks et al. 2013), effectively providing an upper limit on λ_{cs} . Based on other publications (Cassak et al. 2006;

Spangler 2009), an estimate of $\lambda_{cs} = 1.5 \times 10^5$ cm is used, but differing values can certainly be envisioned.

Furthermore, it is convenient to use the reconnecting field B_{rec} instead of the parallel velocity shift Δv_{\parallel} to quantify the current sheet. Valid for the present sinusoidal current sheet configuration, the following expression—stemming from the fundamental equations and verifiable in simulations—relates these two parameters:

$$\frac{B_{rec}}{B_0 \rho_s / L_{ref}} = 3.61 \left(\frac{k_{cs}}{0.4 \rho_s^{-1}} \right)^{-1} \frac{\beta}{0.5} \times \left(\frac{m_e / m_i}{0.01} \right)^{-1/2} \frac{\Delta v_{\parallel}}{0.5 v_{Tj}}. \quad (17)$$

With these ingredients, one can rewrite Equation (10) in cgs units, resulting in a volumetric heating rate:

$$\begin{aligned} \frac{j_{\parallel} E_{\parallel}}{\text{erg cm}^{-3} \text{ s}^{-1}} &= 1.5 \times 10^{-3} \left(\frac{n_{e0}}{10^9 \text{ cm}^{-3}} \right)^{0.375} \left(\frac{T_{e0}}{10^6 \text{ K}} \right)^{-0.1} \\ &\times \left(\frac{L_{ref}}{10^9 \text{ cm}} \right)^{0.2} \left(\frac{\beta}{3.5 \times 10^{-4}} \right)^{0.125} \left(\frac{v_{ei}}{87 \text{ s}^{-1}} \right)^{-0.1} \\ &\times \left(\frac{m_e / m_i}{1/1836} \right)^{-0.25} \left(\frac{T_{i0} / T_{e0}}{1.0} \right)^{0.0} \left(\frac{B_{rec}}{5 \text{ G}} \right)^{1.8} \\ &\times \left(\frac{\tau_{repl}}{1100 \text{ s}} \right)^{-1.5} \left(\frac{\lambda_{cs}}{1.5 \times 10^5 \text{ cm}} \right)^{0.75}. \end{aligned} \quad (18)$$

How does this value compare with observations and other work? In Withbroe & Noyes (1977), the related coronal heating flux is determined to require values on the order of $10^6 \text{ erg cm}^{-2} \text{ s}^{-1}$. It may be translated into a volumetric heating rate via division by the coronal loop length L_{ref} , yielding $10^{-3} \text{ erg cm}^{-3} \text{ s}^{-1}$, in good agreement with Equation (18). Ofman et al. (1998), for $T_{e0} = 10^6 \text{ K}$, reports some $10^{-4} \text{ erg cm}^{-3} \text{ s}^{-1}$, also rather compatible with the present results, while Guarrasi et al. (2014) uses a maximum heating rate of $2 \times 10^{-3} \text{ erg cm}^{-3} \text{ s}^{-1}$, again in good agreement with the findings here.

When recalibrating the focus from the quiet solar corona—for which the physical parameters in Table 2 apply—to active regions or even flares, higher background densities, temperatures, and magnetic fields become of interest. Unless, however, the settings for B_{rec} , τ_{repl} , or λ_{cs} are also changed, the impact of an order-of-magnitude increase in each of the aforementioned background quantities results in an increase of $j_{\parallel} E_{\parallel}$ by less than a factor of two, as per Equation (18). This is not surprising, as the violent event of a solar flare need not necessarily impact the microturbulence that is occurring on smaller length scales. Possible increases in $j_{\parallel} E_{\parallel}$ heating during such events may, however, occur as a consequence of enhanced B_{rec} .

While a number of assumptions have entered into deriving the expression for the heating rate in Equation (18), the fact that its numerical value agrees very well with observational data indicates that the type of reconnection turbulence on which the present work is focused may indeed be contributing a significant fraction to the overall coronal heating.

Most of these parameter dependencies are rather weak, with the strongest impact stemming from the three parameters most closely associated with the current sheet properties: the reconnecting field, the replenishing time, and the sheet width. As mentioned previously, τ_{repl} and λ_{cs} are not well-determined

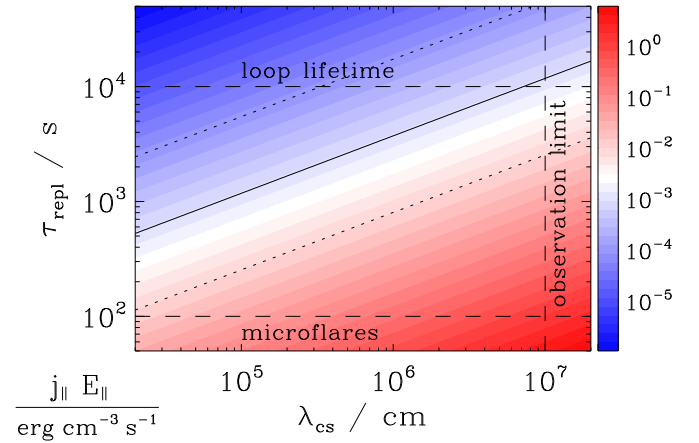


Figure 20. Volumetric heating rate $j_{\parallel} E_{\parallel}$ in units of $\text{erg cm}^{-3} \text{ s}^{-1}$, as a function of current sheet width λ_{cs} and replenishing timescale τ_{repl} . The solid black line denotes a value of 10^{-3} , considered a good estimate for observed heating; for comparison, values of 10^{-4} and 10^{-2} are also included as dotted black lines. Limiting the region of applicable heating rates are the timescales associated with microflares and coronal loop lifetimes, denoted by black dashed lines, as is the spatial resolution limit of present-day observations. Wide ranges of λ_{cs} and τ_{repl} values remain where the present form of reconnection turbulence is able to explain coronal heating.

(A color version of this figure is available in the online journal.)

from observations. Therefore, their impact on $j_{\parallel} E_{\parallel}$ is illustrated in Figure 20, where the heating rate is shown as a function of these two parameters. A wide corridor exists where the observed heating can be explained via $j_{\parallel} E_{\parallel}$ heating due to turbulent reconnection as described in Section 4.

Other previously discussed results that are of interest here are the occurrence of heating bursts in the context of plasmoid mergers and the possibility of these events corresponding to nanoflares. Estimating from Figure 9 that only a few percent of the time-integrated kinetic heating is contained in merger-related bursts—consistent with Figure 12, where nanoflare-relevant mergers occur only at the very highest of energies—the corresponding cgs value becomes a few $10^{-5} \text{ erg cm}^{-3} \text{ s}^{-1}$. This result agrees with the findings of Reale et al. (2005) for averaged heating due to turbulence-born nanoflares, even though the turbulence itself exhibits features very different from those presented here.

It is also most instructive to look at the timescales involved in the plasmoid merger processes. Taking the value $t_{merge} = 2.06 L_{ref} / c_s$ obtained in Section 4 and applying the normalization from Table 2, one arrives at $t_{merge} = 230 \text{ s}$. However, the conditions in the region where observationally relevant nanoflares originate deviate somewhat from those quoted above. As mentioned previously, Parker (1988) contains a discussion of nanoflares; in that publication, somewhat different values are mentioned: $2 \times 10^8 \text{ cm} \lesssim L_{ref} \lesssim 10^9 \text{ cm}$ and $2 \times 10^7 \text{ cm s}^{-1} \lesssim c_s \lesssim 3 \times 10^7 \text{ cm s}^{-1}$. This results in a range for the merge time of $6.7 \text{ s} \lesssim t_{merge} \lesssim 50 \text{ s}$. For the lower end of the quoted range for L_{ref} , observations indicate a nanoflare timescale of $\gtrsim 20 \text{ s}$ (Porter et al. 1984; Parker 1988). It should be noted that in contrast to nanoflares, microflares are described in Parker (1988) as clusters of nanoflares—as a plasmoid merger results in a single, well-identifiable spike in the heating rate, it cannot correspond to an entire microflare with temporal substructure.

Based on the above values, it can therefore be concluded that the simulated t_{merge} agrees rather well with nanoflare timescales from observations. However, an important caveat is to be made:

t_{merge} was measured in a simulation at parameters that require some rescaling to match coronal conditions. The agreement observed here is conditional either on t_{merge} not varying with those input parameters or on various dependencies of t_{merge} effectively canceling. Considering the findings of Section 4, this may well be the case, but additional simulation work will have to be conducted to achieve a greater degree of certainty in this matter.

7. SUMMARY

Magnetic reconnection turbulence—i.e., turbulence driven by reconnection but also itself creating new reconnection—has been studied in the strong guide field limit, via gyrokinetic simulations. The drive was provided through a current sheet in the y direction (which is replenished continuously), thus creating a system susceptible to the tearing instability. An important characteristic of the resulting turbulence is the emergence of circular structures in the parallel current identified as plasmoids; these objects are subject to forces that cause mutual attraction between currents of the same sign and may result in mergers of two plasmoids. Such events cause bursts in the heating rate, and their characteristic timescale suggests that plasmoid mergers may be the cause of solar nanoflares.

Heating, at nominal parameters, is dominated by kinetic processes, with the $j_{\parallel}E_{\parallel}$ heating primarily stemming from a flutter-like component that directs \mathbf{E}_{\perp} fluctuations, which are perpendicular to the perturbed field lines, along the guide field. Using nonlinear parameter scans, a parameterization for the heating rate is provided, and it is shown that kinetic heating significantly exceeds collisional heating for Lundquist numbers above the plasmoid threshold of 10^4 . The results also indicate that linear tearing mode physics cannot fully explain the measured scalings, to which the nonlinear cascade contributes additional features. When applying parameters typical for solar corona plasmas to the simulations, it is shown that the resulting volumetric heating rate of $1.5 \times 10^{-3} \text{ erg cm}^{-3} \text{ s}^{-1}$ —while subject to some uncertainty due to a number of assumptions—is in good quantitative agreement with the situation in the corona, as illustrated in Figure 20. It is therefore concluded that turbulence of the type studied here may constitute an important process in coronal heating.

Additionally, it is demonstrated that tearing mode physics is able to produce temperature anisotropies in the absence of background anisotropy. While ordering considerations require those anisotropies to be small relative to the stable equilibrium, as a secondary process, tearing modes and reconnection turbulence are identified as a candidate cause of solar ion anisotropy in cases where no cyclotron-resonant heating occurs.

Future investigations will have to address, among other matters, two questions: Do additional turbulence regimes exist where the scalings derived here break down? And do dependencies exist of the plasmoid merger rate on various input parameters? In addition, the existence of background gradients in the density and temperature is able to significantly alter the characteristics of the turbulence, and future work will have to determine to what degree such gradients are able to influence plasma microturbulence in the corona.

Lastly, the effects of fully resolving the third spatial dimension—in the form of the coordinate z along the background magnetic field—will have to be investigated. In addition to extending the corresponding preliminary studies mentioned in the present paper, current sheets with helicity will have to be analyzed. Past studies (Borgogno et al. 2005; Perona et al. 2014)

indicate that magnetic islands become asymmetric under the influence of finite helicity and that stochastic magnetic fields may reduce driving current gradients. It may be speculated that in a fully turbulent state, such asymmetries are mitigated, while stochasticity may, depending on its strength, impact plasmoid amplitudes.

The authors are particularly grateful to D. R. Hatch, R. Numata, D. Carmody, S. Boldyrev, N. Loureiro, and W. Daughton for valuable input. Support for this work was provided by the National Science Foundation. Funding has been received from the European Research Council under the European Union's Seventh Framework Programme (FP7/2007–2013)/ERC Grant Agreement No. 277870.

REFERENCES

- Alexandrova, O., Saur, J., Lacombe, C., et al. 2009, *PhRvL*, **103**, 165003
 Bale, S. D., Kasper, J. C., Howes, G. G., et al. 2009, *PhRvL*, **103**, 211101
 Bañón Navarro, A., Morel, P., Albrecht-Marc, M., et al. 2011a, *PhPI*, **18**, 092303
 Bañón Navarro, A., Morel, P., Albrecht-Marc, M., et al. 2011b, *PhRvL*, **106**, 055001
 Benz, A. O., & Krucker, S. 2002, *ApJ*, **568**, 413
 Bhattacharjee, A., Huang, Y.-M., Yang, H., & Rogers, B. 2009, *PhPI*, **16**, 112102
 Biskamp, D. 1986, *PhFl*, **29**, 1520
 Boldyrev, S., & Perez, J. C. 2012, *ApJL*, **758**, L44
 Borgogno, D., Grasso, D., Porcelli, F., et al. 2005, *PhPI*, **12**, 032309
 Brizard, A. J., & Hahm, T. S. 2007, *RvMP*, **79**, 421
 Brooks, D. H., Warren, H. P., Ugarte-Urra, I., & Winebarger, A. R. 2013, *ApJL*, **772**, L19
 Burkhart, G. R., & Chen, J. 1989, *PhRvL*, **63**, 159
 Candy, J., Waltz, R. E., Parker, S. E., & Chen, Y. 2006, *PhPI*, **13**, 074501
 Carmody, D., Puschel, M. J., & Terry, P. W. 2013, *PhPI*, **20**, 052110
 Cassak, P. A., & Drake, J. F. 2013, *PhPI*, **20**, 061207
 Cassak, P. A., Drake, J. F., & Shay, M. A. 2006, *ApJL*, **644**, L145
 Cassak, P. A., & Shay, M. A. 2012, *SSRv*, **172**, 283
 Chen, C. H. K., Salem, C. S., Bonnell, J. W., et al. 2012, *PhRvL*, **109**, 035001
 Chen, J., Palmadesso, P. J., Fedder, J. A., & Lyo, J. G. 1984, *GeoRL*, **11**, 12
 Comisso, L., Grasso, D., Tassi, E., & Waelbroeck, F. L. 2012, *PhPI*, **19**, 042103
 Comisso, L., Grasso, D., Waelbroeck, F. L., & Borgogno, D. 2013, *PhPI*, **20**, 092118
 Connor, J. W., Cowley, S. C., & Hastie, R. J. 1990, *PPCF*, **32**, 799
 Cranmer, S. R. 2001, *JGR*, **106**, 24937
 Cranmer, S. R., van Ballegoijen, A. A., & Edgar, R. J. 2007, *ApJS*, **171**, 520
 Daughton, W., Roytershteyn, V., Albright, B. J., et al. 2009, *PhRvL*, **103**, 065004
 Daughton, W., Roytershteyn, V., Karimabadi, H., et al. 2011, *NatPh*, **7**, 539
 Donato, S., Servidio, S., Dmitruk, P., et al. 2013, in *AIP Conf. Proc.* 1539, *Solar Wind 13*, ed. G. P. Zank et al. (Melville, NY: AIP), 99
 Drake, J. F., Swisdak, M., Phan, T. D., et al. 2009, *JGR*, **114**, A05111
 Drake, J. F., Swisdak, M., Schoeffler, K. M., et al. 2006, *GeoRL*, **33**, L13105
 Einaudi, G., & Van Hoven, G. 1981, *PhFl*, **24**, 1092
 Fermo, R. L., Drake, J. F., & Swisdak, M. 2012, *PhRvL*, **108**, 255005
 Fitzpatrick, R. 2010, *PhPI*, **17**, 042101
 Frieman, E. A., & Chen, L. 1982, *PhFl*, **25**, 502
 Furth, H. P., Killeen, J., & Rosenbluth, M. N. 1963, *PhFl*, **6**, 459
 Görler, T. 2009, PhD thesis, Univ. Ulm
 Grasso, D., Tassi, E., & Waelbroeck, F. L. 2010, *PhPI*, **17**, 082312
 Guarrasi, M., Reale, F., Orlando, S., et al. 2014, *A&A*, **564**, A48
 Hannah, I. G., Christe, S., Krucker, S., et al. 2008, *ApJ*, **677**, 704
 Hesse, M., Schindler, K., Birn, J., & Kuznetsova, M. 1999, *PhPI*, **6**, 1781
 Hirzberger, J., Bonet, J. A., Vázquez, M., & Hanslmeier, A. 1999, *ApJ*, **515**, 441
 Hollweg, J. V., & Isenberg, P. A. 2002, *JGR*, **107**, 1147
 Howes, G. G., Dorland, W., Cowley, S. C., et al. 2008, *PhRvL*, **100**, 065004
 Huang, Y.-M., & Bhattacharjee, A. 2010, *PhPI*, **17**, 062104
 Huang, Y.-M., & Bhattacharjee, A. 2013, *PhPI*, **20**, 055702
 Hudson, H. S. 1991, *SoPh*, **133**, 357
 Ishizawa, A., & Watanabe, T.-H. 2013, *PhPI*, **20**, I02116
 Jenko, F., Dorland, W., Kotschenreuther, M., & Rogers, B. N. 2000, *PhPI*, **7**, 1904
 Karimabadi, H., Daughton, W., & Quest, K. B. 2005, *JGR*, **110**, A03214
 Karimabadi, H., Roytershteyn, V., Daughton, W., & Liu, Y.-H. 2013, *SSRv*, **178**, 307

- Kobayashi, S., Rogers, B. N., & Numata, R. 2014, *PhPI*, **21**, 040704
- Kohl, J. L., Noci, G., Antonucci, E., et al. 1997, *SoPh*, **175**, 613
- Kohl, J. L., Noci, G., Antonucci, E., et al. 1998, *ApJL*, **501**, L127
- Lazarian, A., Kowal, G., Vishniac, E., & de Gouveia Dal Pino, E. 2011, *P&SS*, **59**, 537
- Lazarian, A., Vlahos, L., Kowal, G., et al. 2012, *SSRv*, **173**, 557
- López Fuentes, M. C., Klimchuk, J. A., & Mandrini, C. H. 2007, *ApJ*, **657**, 1127
- Loureiro, N. F., Schekochihin, A. A., & Cowley, S. C. 2007, *PhPI*, **14**, 100703
- Loureiro, N. F., Schekochihin, A. A., & Zocco, A. 2013, *PhRvL*, **111**, 025002
- Loureiro, N. F., Uzdensky, D. A., Schekochihin, A. A., et al. 2009, *MNRAS*, **399**, L146
- Marsch, E., Mühlhäuser, K.-H., Schwenn, R., et al. 1982, *JGR*, **87**, 52
- Matsui, T., & Daughton, W. 2008, *PhPI*, **15**, 012901
- Mehlretter, J. P. 1978, *A&A*, **62**, 311
- Neukirch, T. 1996, in ASP Conf. Ser. 111, Magnetic Reconnection, in the Solar Atmosphere, ed. R. D. Bentley & J. T. Mariska (San Francisco, CA: ASP), **286**
- Ng, C. S., Lin, L., & Bhattacharjee, A. 2012, *ApJ*, **747**, 109
- Numata, R., Dorland, W., Howes, G. G., et al. 2011, *PhPI*, **18**, 112106
- Ofman, L., Klimchuk, J. A., & Davila, J. M. 1998, *ApJ*, **493**, 474
- Ottaviani, M., Arcis, N., Escande, D. F., et al. 2004, *PPCF*, **46**, B201
- Parker, E. N. 1988, *ApJ*, **330**, 474
- Paschmann, G., Øieroset, M., & Phan, T. 2013, *SSRv*, **178**, 385
- Perona, A., Borgogno, D., & Eriksson, L.-G. 2014, *CoPhC*, **185**, 86
- Perona, A., Eriksson, L.-G., & Grasso, D. 2010, *PhPI*, **17**, 042104
- Plunk, G. G., Tatsuno, T., & Dorland, W. 2012, *NJPh*, **14**, 103030
- Porcelli, F. 1991, *PhRvL*, **66**, 425
- Porter, J. G., Toomre, J., & Gebbie, K. B. 1984, *ApJ*, **283**, 879
- Predebon, I., & Sattin, F. 2013, *PhPI*, **20**, 040701
- Priest, E. R., & Forbes, T. G. 2002, *A&ARv*, **10**, 313
- Pritchett, P. L. 2006, *JGR*, **111**, A10212
- Pueschel, M. J., Hatch, D. R., Görler, T., et al. 2013, *PhPI*, **20**, 102301
- Pueschel, M. J., Jenko, F., Schneller, M., et al. 2012, *NucFu*, **52**, 103018
- Pueschel, M. J., Jenko, F., Told, D., & Büchner, J. 2011, *PhPI*, **18**, 112102
- Rappazzo, A. F., & Velli, M. 2011, *PhRvE*, **83**, 065401
- Reale, F., Nigro, G., Malara, F., et al. 2005, *ApJ*, **633**, 489
- Rechester, A. B., & Rosenbluth, M. N. 1978, *PhRvL*, **40**, 38
- Rogers, B. N., Kobayashi, S., Ricci, P., et al. 2007, *PhPI*, **14**, 092110
- Rogers, B. N., Kobayashi, S., Ricci, P., et al. 2011, *PhPI*, **18**, 049902
- Scharmer, G. B., Narayan, G., Hillberg, T., et al. 2008, *ApJL*, **689**, L69
- Schekochihin, A. A., Cowley, S. C., Dorland, W., et al. 2009, *ApJS*, **182**, 310
- Servidio, S., Matthaeus, W. H., Shay, M. A., et al. 2009, *PhRvL*, **102**, 115003
- Spangler, S. R. 2009, *NPGeo*, **16**, 443
- Swisdak, M., Rogers, B. N., Drake, J. F., & Shay, M. A. 2003, *JGR*, **108**, 1218
- TenBarge, J. M., Daughton, W., Karimabadi, H., et al. 2014, *PhPI*, **21**, 020708
- TenBarge, J. M., & Howes, G. G. 2013, *ApJL*, **771**, L27
- Tu, C.-Y., & Marsch, E. 2001, *JGR*, **106**, 8233
- Uzdensky, D. A., Loureiro, N. F., & Schekochihin, A. A. 2010, *PhRvL*, **105**, 235002
- von Steiger, R., & Zurbuchen, T. H. 2003, in AIP Conf. Proc. 679, Solar Wind Ten, ed. M. Velli, R. Bruno, & F. Malara (Melville, NY: AIP), **526**
- Vranjes, J., Poedts, S., & Ehsan, Z. 2009, *PhPI*, **16**, 074501
- Wan, W., Chen, Y., & Parker, S. E. 2005, *PhPI*, **12**, 012311
- Wang, X. Y., Lin, Y., Chen, L., & Lin, Z. 2008, *PhPI*, **15**, 072103
- Winebarger, A. R., Warren, H. P., & Seaton, D. B. 2003, *ApJ*, **593**, 1164
- Withbroe, G. L., & Noyes, R. W. 1977, *ARA&A*, **15**, 363
- Yamada, M., Kulsrud, R., & Ji, H. 2010, *RvMP*, **82**, 603
- Zacharias, O., Kleiber, R., & Hatzky, R. 2012, *JPhCS*, **401**, 012026
- Zharkova, V. V., Arzner, K., Benz, A. O., et al. 2011, *SSRv*, **159**, 357
- Zweibel, E. G., Lawrence, E., Yoo, J., et al. 2011, *PhPI*, **18**, 111211
- Zweibel, E. G., & Yamada, M. 2009, *ARA&A*, **47**, 291